

**Effect of Abolition of Intersubunit Salt Bridges on Allosteric Protein Structural Dynamics**

Journal:	<i>Chemical Science</i>
Manuscript ID	SC-EDG-03-2021-001207.R1
Manuscript Type:	Edge Article
Date Submitted by the Author:	23-Apr-2021
Complete List of Authors:	Ihee, Hyotcherl; KAIST Choi, Minseo; KAIST Kim, Jong Goo; KAIST Muniyappan, Srinivasan; KAIST Kim, Hanui; KAIST Kim, Tae Wu; KAIST Lee, Yunbeom; KAIST Lee, Sang Jin; KAIST Kim, Seong Ok; Institute for Basic Science (IBS)

SCHOLARONE™
Manuscripts

Chemical Science

Guidelines for Referees

Thank you very much for agreeing to review this manuscript for *Chemical Science*.

Chemical
Science



© ROYAL SOCIETY OF CHEMISTRY

Chemical Science is the flagship journal from the Royal Society of Chemistry publishing findings from across the breadth of the chemical sciences.

Articles should be of exceptional significance to their field, which would also be of wider interest to readers working in other areas across the chemical sciences.

Chemical Science's Impact Factor is 9.346 (2019 Journal Citation Reports®)

The following manuscript has been submitted for consideration as an
EDGE ARTICLE

For acceptance, an Edge article must report primary research which provides a significant new concept, advance or insight into the development of its field, and be of interest to scientists across the broad multi-disciplinary readership of the journal. There are no page limits for Edge articles, so authors can choose how best to present their research. However Electronic Supplementary Information (ESI) is recommended for additional data and experimental details.

We ask referees to **recommend only the most significant work** for publication in *Chemical Science*. When making your recommendation please:

- **Comment on** the novelty and significance to the field, the broader appeal and scientific reliability.
- **Note that routine or incremental** work should not be recommended for publication.
- **Contact the Associate Editor** if there is any conflict of interest, if the work has been previously published or if there is a significant part of the work which you are not able to referee with confidence.

Best regards,

Andrew Cooper

May Copsey

Contact us

Professor Andrew Cooper

Editor-in-Chief, *Chemical Science*

Dr May Copsey

Executive Editor, *Chemical Science*

Please visit our [reviewer hub](#) for further details of our processes, policies and reviewer responsibilities as well as guidance on how to review, or click the links below.



What to do
when you
review



Reviewer
responsibilities



Process &
policies

Dear Editor,

We appreciate your consideration of our manuscript titled “Effect of Abolition of Intersubunit Salt Bridges on Allosteric Protein Structural Dynamics” and the constructive comments from the reviewers. We have revised our manuscript to address the concerns and suggestions raised by the reviewers. The original comments by the reviewers in italic are followed by arrows with our responses. In addition, we also made several minor changes to improve the readability of the manuscript. We are submitting an annotated version of our manuscript where all the changes we have made in the main text and the SI are indicated using the “Track Changes” function in Microsoft Word.

Thank you for your consideration and we look forward to hearing about your decision.

Sincerely,

Hyotcherl Ihee

Professor, Department of Chemistry, KAIST
291 Daehak-ro, Yuseong-gu
Daejeon 34141, Republic of Korea
(Tel) +82-42-350-2844
(Fax)+82-42-350-2810
(Email) hyotcherl.ihee@kaist.ac.kr

Responses to the comments from Reviewer #1

The homodimeric hemoglobin (HbI) studied here is an excellent model system for exploring issues of allosteric protein structural dynamics by time resolved X-ray solution scattering. This group has already gained substantial insight investigating wild-type and several very interesting mutants. The interpretation requires extensive analysis, with some assumptions, but this group is very well qualified for such analysis.

→ We thank the reviewer's constructive comments. In the following, we tried to address the reviewer's concerns.

The previous analysis of the HbI involved wild-type and mutants that maintain the dimeric assembly during its structural transitions. As a result, all of the X-scattering observed in the time-resolved solution scattering experiments emanate from conformations within the context of the dimer. However, the K30D mutation studied here has been shown to substantially weaken the dimeric interface to the point that the binding properties and structural transitions will be strongly concentration dependent. For instance, as shown by Ceci et al., 2002 (ref. 26), at a protein concentration of 12 uM, the protein is primarily monomeric and binds oxygen non-cooperatively with high affinity ($p_{50}=1.5$ Torr). At higher concentrations (~800 uM), oxygen binding shows similar properties to wild-type HbI with cooperativity (Hill coefficient 1.35) and lower affinity ($p_{50}=7.6$ Torr). Thus, the structural transitions that occur in the K30D are dependent upon the protein concentration, with higher concentrations demonstrating cooperative oxygen binding characteristics similar to that of wild-type, whereas lower concentration experiments apparently show the characteristics of monomeric subunits. This adds a complexity to analysis of K30D and also suggests performing experiments at various protein concentrations may be useful for sorting out such complexities.

→ We thank the reviewer for this suggestion, but it should be noted that collecting even a single TRXSS data set with a sufficient number of time delays (33 time delays) and sufficient signal-to-noise ratios at all time delays is still a challenge. For this reason, for a typical TRXSS experiment, we screen for the optimal concentration and tackle the complexity referred by the reviewer with the elaborate data analysis. The concentration used in this work (2.3 mM) is higher than 800 uM, which is the concentration where K30D shows similar cooperativity to WT, according to a previous work (Ceci. et al., 2002 (ref. 26)). We conducted the TRXSS experiment at this concentration to maximize the signal contribution of dimers without suffering from aggregation at high concentrations. Even in retrospect, this choice of

concentration seems optimal. If TRXSS data were obtained at various concentrations, it would certainly increase information content, as the reviewer suggested. For example, if a TRXSS data is obtained at a very low concentration where the cooperativity is lost such as 12 uM, probably only monomers will contribute to the scattering signal. At 2.3 mM, the data show a mixture of monomers and dimers, making the analysis complicated. Nevertheless, we believe that our analysis is successful in overcoming the complexity.

The authors in this study found that the kinetic analysis required four structural intermediates, rather than the three intermediates obtained with their previous wild-type and mutant analysis. As the authors point out, “the fit quality alone cannot discriminate whether the fourth species is a dimer or a monomer”. With a logical analysis, the authors conclude that the fourth species most likely corresponds to a monomer. Most strikingly, the monomer appears to account for over 80% of the species present. Given that, the time constants derived for CO rebinding to the monomer are probably quite accurate. However, the point of the paper is to provide insight into the allosteric structural transitions which only occur in the dimer. It seems to me that here the authors are on much shakier ground, given that they are trying to make an analysis on a species that is contributing to less than 20% of the scattering. For instance, the authors claim that the analysis shows that salt bridges in HbI may play a functional role in ligand binding as well as the structural role contributing to the R-T allosteric transition. This is a counter-intuitive conclusion, given the location of the salt bridge near the periphery of the dimer and the previous data.

In order to be convincing, I think the data would need to be much stronger and not based on extensive fitting and modelling of less than 20% of the contribution to the measured X-ray scattering data.

→ We thank the reviewer for this comment as it prompted us the need to add a discussion on this point and helped us improve the manuscript (see below). It is correct that the relative portion of dimers in terms of the concentration that contributes to the difference scattering signal is 20% (and that of monomers is 80%), but this does not mean that the relative contribution to the difference scattering signal is 20%. One dimer contributes more strongly to the scattering signal than one monomer does because a dimer is twice heavier than a monomer and a dimer has a larger structural change than a monomer. The scales of the SADSSs in Fig. 3B were adjusted to show the difference scattering curve per one molecule (either dimer or monomer). If the actual concentrations are multiplied to these SADSSs, the actual contribution

to the signal can be quantitatively shown. For this purpose, we made a new figure showing the SADSs multiplied by the maximum concentrations of the four species (see the left panel of the figure below, Fig. S12). This figure confirms that the contribution of dimers is comparable to that of monomers. More importantly, the magnitudes of SADSs are substantially larger than the noise level, indicating that the signal-to-noise ratio of the current data is enough to provide information for both dimers and monomers. Besides, we made another new figure showing the relative contributions of dimers and monomers to the difference scattering signal as a function of time (see the right panel of the figure below). The figure shows that the relative contribution of dimers ranges from 25% to 88%.

Considering the reviewer's comment, we added the following discussion to the revised manuscript.

"We note that the relative portion of dimers in terms of the concentration that contributes to the difference scattering signal is ~20% (and that of monomers is ~80%), but this does not mean that the relative contribution to the difference scattering signal is 20%. One dimer contributes more strongly to the scattering signal than one monomer because a dimer is twice heavier than a monomer and a dimer generally has a larger structural change than a monomer. The relative contributions of dimers to the difference signal range from 25% to 88% depending on time, as shown in Fig. S12."

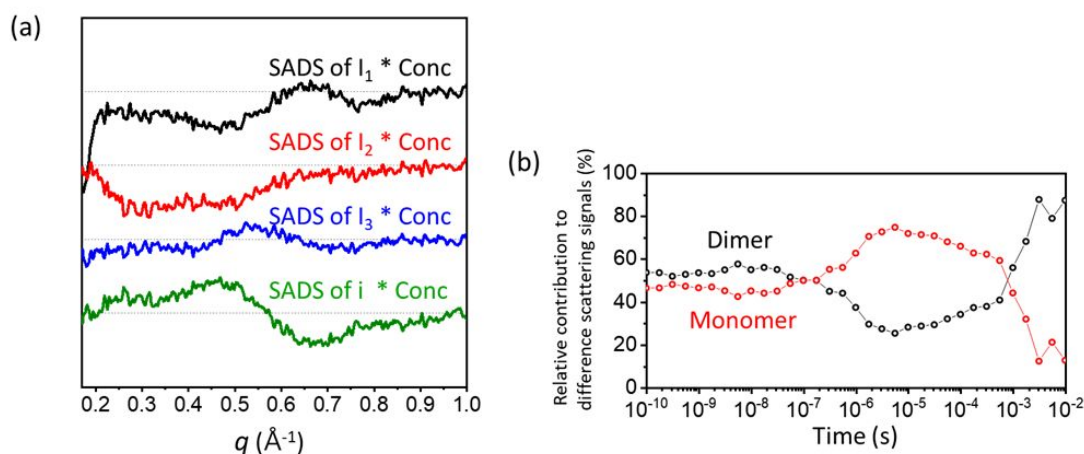


Fig. S12. (a) SADSs multiplied by the maximum concentrations of the four species (0.70 mM for I_1 , 0.64 mM for I_2 , 0.72 mM for I_3 , and 2.91 mM for i). This figure confirms that the contribution of dimers is comparable to that of monomers. More importantly, the magnitudes of SADSs are substantially larger than the noise level, indicating that the signal-to-noise ratio of the current data is enough to provide information for both dimers and monomers. (b) The

relative contributions of dimers and monomers to the difference scattering signals as a function of time.

Regarding the counter-intuitive conclusion referred by the reviewer, indeed the salt bridges are located near the interface whereas the heme group where the ligand-binding occurs is located near the center of the subunit. We did not suggest that the salt bridges themselves play a direct role in the ligand binding itself. Rather, we suggested that the data analysis showed that the salt bridges play a functional role in the ligand binding via its allosteric structural role contributing to the progression of R-T allosteric structural transition. Related to this point, it is known that the dimer interface where the salt bridges are located not only is involved in the structural connection of the subunits but also acts as a bridge conveying a structural change of one subunit to the other subunit, playing a critical role in the allosteric structural regulation. For example, previous studies reported that the distal histidine located in the interface of HbI acts as a gate for the ligand and the entry and exit of the ligand can involve a concerted rearrangement of groups in the interface (*Structure*, 2009, **17**, 1494-1504, and *Biochemistry*, 2007, **46**, 14018–14031).

Considering the reviewer's comment, we added the following discussion to the revised conclusion.

“The comparisons of the structural dynamics and kinetics of K30D and WT offer insights into the role of salt bridges. If interfacial salt bridges serve only as structural constraints to increase the rigidity between two subunits, one may expect that K30D, where the salt bridges are abolished, would have a more flexible intersubunit motion than WT. The data show the opposite; K30D has a suppressed intersubunit motion, suggesting a more sophisticated role of interfacial salt bridges beyond a simple structural glue between subunits. It should be noted that the structural changes of HbI are closely related to allosteric regulation. Once a ligand is attached to the heme of one subunit, this may trigger the change of the ligand-binding affinity of the other subunit via allosteric regulation. This consideration renders that the interfacial salt bridges not only assist the physical connection of two subunits but also play a critical role in the global structural signal transduction of one subunit to the other subunit via a series of well-organized structural transitions.”

If the goal of the manuscript was to understand the properties of the dimer, rather than an isolated subunit, I am surprised that the authors didn't do more to increase the proportion of

the dimer in their experiments. For instance, although they are at quite high a concentration (2-4mM) hemoglobin is a very soluble protein and it may be possible to get HbI at a higher concentration for such experiments. Alternatively, the authors suggest that the increased dimer dissociation results because of the higher temperature of their analysis, but show no data that going from 10C to 20C would have that strong a change. If they are correct, can they lower the temperature of their X-ray scattering experiment?

→ As the reviewer pointed out, a higher concentration could increase the ratio of the dimer. However, there are experimental limitations, as we answered in the previous question. In short, at high concentrations, interparticle correlation and protein aggregation can affect the TRXSS signal, so that the concentration can be increased only to the extent that these problems do not occur in typical TRXSS experiments. The concentration of 2.3 mM we used in this work was determined by considering those issues. We note that the TRXSS data measured at this concentration have a sufficiently enough signal-to-noise ratio to extract the kinetic and structural information of the dimer intermediates, as we mentioned in the previous answer. Thus, we believe that the structural dynamics for the dimer revealed in this study are reliable. The idea of controlling the temperature the reviewer mentioned can be another good option for altering the monomer-dimer equilibrium. But any low-temperature TRXSS data on WT HbI has not been reported. For this reason, for the primary goal of confirming how the structural dynamics of HbI are affected by the presence or absence of salt bridges, the experiment on K30D was conducted at the same temperature at which the TRXSS experiments on WT and other mutants were conducted.

In its present form, I do not think that the experiments presented convincingly demonstrate the conclusions that they are making.

→ We hope that our answers may have helped to clear out potential misunderstandings and doubts. We respect the reviewer's suggestion for further experiments at a wider range of concentrations, but we believe that our analysis and conclusion are sufficient in conveying the key insights obtained from analyzing the data at a single concentration.

Responses to the comments from Reviewer #2

The Ihee group have a long history on studying the photo-induced kinetics of homodimeric hemoglobins (wild type and mutants) using time-resolved solution x-ray scattering technique. In this manuscript, Ihee and co-workers studied a K30D mutant, in which the interfacial salt bridges of wild type are abolished. The study revealed that kinetics and structures of intermediates changed due to the absence of the salt bridges, which is relevant to the protein function. This is a piece of good data on the effects of salt bridges on protein functions. The data analyses are solid and the interpretations are sound.

I would recommend publish this manuscript after addressing the following minor points:

→ We thank the reviewer for the positive evaluation of our work. In the following, we tried to address the reviewer's comments.

(1) *Man text, Page 11, paragraph 1: “The size of the x-ray beam was adjusted to be 0.90 × 0.70 mm² at the sample, which is smaller than the laser spot size,” Is it a typo? Because in a previous sentence says the laser spot is 015x0.60 mm².*

→ We appreciate the reviewer's careful review. The x-ray beam was focused to a spot of 0.09 × 0.07 mm² at the sample position. We corrected the typo in the revised manuscript.

(2) *SI, page 31, a typo of an eqn in “This fitted curve, represented by a linear combination of () and () , was subtracted from the difference curves at all time delays to remove the solvent heating effect”*

→ We appreciate the reviewer's careful review. The process was performed using a linear combination of the scattering signal arising from the temperature change at a constant density, $((\partial S(q)/\partial T)_\rho)$, and the density change at a constant temperature, $((\partial S(q)/\partial \rho)_T)$. We corrected the typo.

(3) *SI, page 33. “The contribution from the fourth singular vector and beyond becomes negligible.” “The fourth” should be “the fifth”.*

→ We appreciate the reviewer's careful review. We corrected the typo.

Responses to the comments from Reviewer #3

The manuscript by Ihee, et al. describes the analysis by time-resolved X-ray solution scattering (TRXSS) of a mutant (K30D) of dimeric hemoglobin undergoing photoinduced ligand dissociation and subsequent rebinding. Dimeric hemoglobin is a model system for understanding allosteric transitions in proteins, which are still poorly understood from a structural perspective. The K30D mutant is interesting, as it abolishes a key intersubunit salt bridge thought to be important for allosteric communication between the subunits. The authors aim to understand how this mutation compromises the dynamics of the enzyme, thus dissecting the role of the associated salt bridge in protein motions that underlie allostery.

The authors have a long history of studying the structural dynamics of hemoglobins, myoglobins, and other photoactivated systems using various time-resolved methods, including TRXSS, and they have made numerous technical and scientific contributions to this field. Consistent with their previous work, the data presented here appear to be expertly collected and analyzed using state-of-the-art methods. In particular, this work utilizes an interesting monte-carlo structural modeling approach that seems especially useful in the context of modeling intersubunit rearrangements.

→ We appreciate the reviewer's positive evaluation of our work. In the following, we tried to address the reviewer's comments.

Kinetic modeling of structural transitions from TRXSS data is always complex and requires numerous assumptions, and the case here is no different. It should be noted that the problem that the authors are tackling is extremely challenging. The kinetic schemes proposed by the authors (Fig. 3) are generally logical based on their kinetic SVD analysis and what is known for other dimeric hemoglobin variants, including WT, but they have some potential weaknesses as well. For example, there are some ambiguities in the models, which are noted in earnest by the authors and addressed in the SI. Additionally, due to the lack of a T-like state and the weakness of the contribution of the fourth singular vector to the overall scattering signal, I wonder if the analysis of this particular mutant might require a more dramatic departure from the I1, I2, I3 model used for other variants of dimeric hemoglobin? (Regarding the fourth singular vector – Fig. S9 shows that its singular value approaches the noise floor, and neither the lSV or the rSV has a particularly convincing shape, in my opinion. Its interpretation doesn't go as far as raising red flags for me, but I am somewhat skeptical.)

→ First of all, regarding the 4th SVD component, although it is noisier than the other three components, $s_4 \times 4^{\text{th}} \text{rSV}$, which represents the actual contribution to the signal, shows non-zero contributions as a function of time (please see the figure below, Fig. R1). Especially, the contribution after $1 \mu\text{s}$ is significant and the $s_4 \times 4^{\text{th}} \text{rSV}$ curve can be fit with a set of apparent time constants common for all four components. We notice that the old Fig. 2c showing these rSVs multiplied by singular values does not show this well, and thus we replace the old Fig. 2c with the new one. Moreover, if only three SVD components are used for the kinetic analysis by dropping out the 4th component (for example, if the kinetic framework containing only I_1 , I_2 , and I_3 without i is used), the fit quality degrades significantly; The chi-square value increases by 21%. Related to this, we added another new figure (Fig. S13) showing the fit quality with only three components without the 4th component.

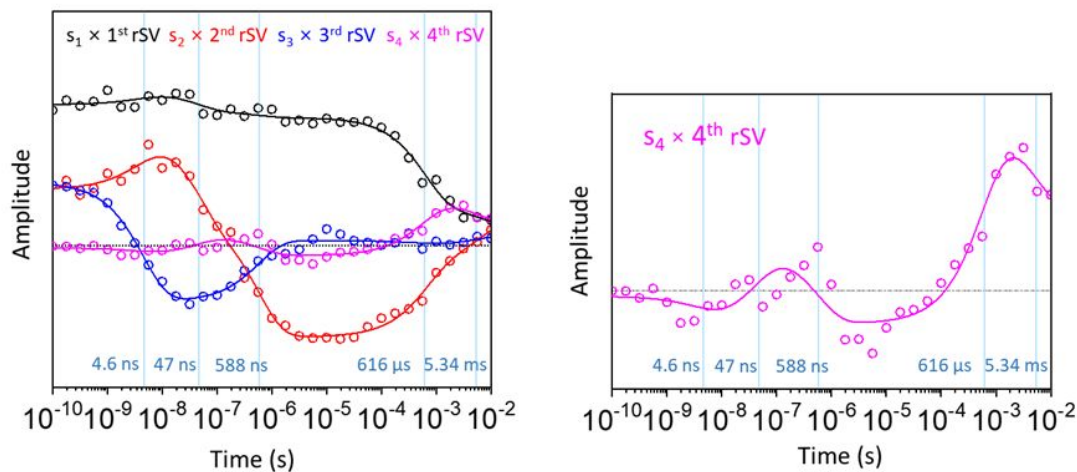


Fig. R1. (Left) New Fig. 2c replacing the old Fig. 2c. (Right) The magnified view of the 4th rSV multiplied by the corresponding singular value (magenta open circles) and its fit (a magenta curve) using a sum of exponential functions with the time constants of 4.6 ns, 47 ns, 588 ns, $616 \mu\text{s}$, and 5.34 ms.

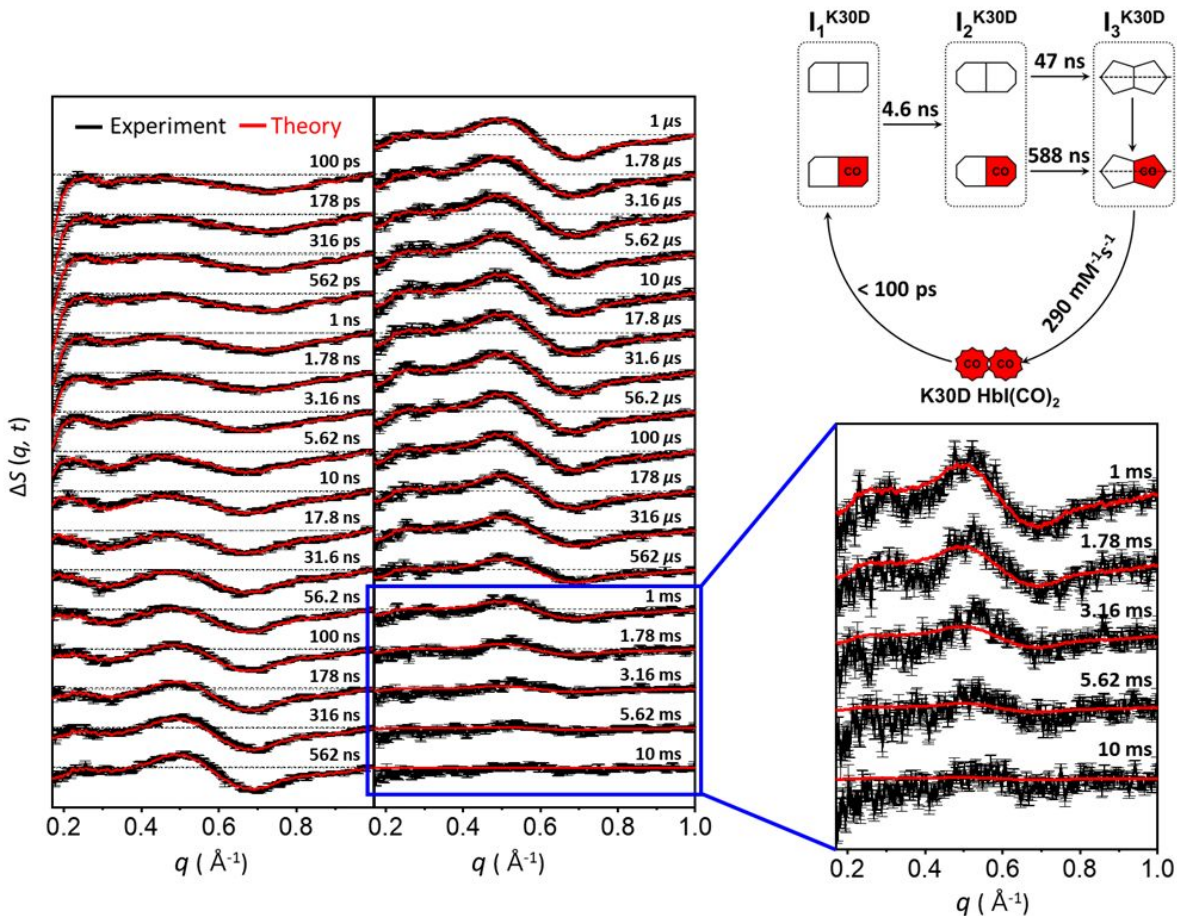


Fig S13. Time-resolved x-ray solution scattering curves, $\Delta S(q, t)$, measured for a solution sample of K30D (black curves) are compared with theoretical curves (red curves) generated by linear combinations of only three ISVs instead of four, based on the kinetic model with only three dimer intermediates (I_1 , I_2 , and I_3) without the monomer intermediate (i). Note that the fit quality is significantly worse than those including the fourth intermediate in Fig. S2. The chi-square value increases by 21%.

More importantly, regarding the reviewer's suggestion to consider a more dramatic departure from the kinetic framework of WT, this comment made us realize that readers may have similar questions and doubts about the certainty of the kinetic framework. In the revised manuscript, we added a more detailed discussion with a more systematic and heuristic description of how the number of kinetic frameworks was narrowed down and how the final kinetic model was determined (see below).

As the reviewer correctly pointed out, this issue is not trivial, and our group has tried to advance on this front over many years. In short, two methods greatly help us narrow down

the kinetic models compatible with the experimental data: (i) the numbers of species from the SVD results on various reduced time ranges and (ii) SVD-aided pseudo PCA analysis (SAPPA) (*Struct. Dyn.*, 2017, **4**, 044013). With this said, in the original manuscript, we indeed tried to stick to the general framework common to WT and all mutants (F97Y, T72V, and I114F) studied with TRXSS so far. For this reason, we adopted the biphasic I₂-to-I₃ transition. Now, upon the reviewer's request to consider other wilder possibilities, we mention the possibility of the following additional frameworks (see the figure below). In this process, we added a more detailed discussion using the SAPPA method. Accordingly, we modified the related discussion and added the following discussion in the SI. We note that this new discussion is also intended as our detailed answer to the reviewer's comment.

"To establish the kinetic framework, we used two effective methods that can greatly facilitate narrowing down the kinetic models compatible with the experimental data: (i) the numbers of species from the SVD results on various reduced time ranges and (ii) SVD-aided pseudo PCA analysis (SAPPA)(ref). First of all, we obtained clues about the number of intermediates associated with each of the relaxation times by performing the SVD analyses for various reduced time ranges in addition to the whole data.¹ For the SVD with a reduced time range, the upper limit close to and containing the value of each time constant obtained from the fitting of rSVs was chosen. Accordingly, four reduced time ranges (i) from 100 ps to 5.62 ns, (ii) from 100 ps to 56.2 ns, (iii) from 100 ps to 1 μ s, and (iv) from 100 ps to 1 ms were used for SVD analysis. The major lSVs from the SVD analysis for reduced and the entire ranges are shown in Fig. S10. The SVD result shows that the first time range from 100 ps to 5.62 ns has two main components, indicating that the first time constant of 4.61 ns can be explained as contributing to the transition from the first intermediate (A) to the second intermediate (B). The SVD results on the second time range from 100 ps to 56.2 ns and the third range from 100 ps to 1 μ s reveal that the number of main components increases to and remains at three. Adding the third intermediate (C) satisfying this condition allows for the nine kinetic frameworks shown in Fig. S14.

To further narrow down the kinetic frameworks compatible with the experimental data, we used the SAPPA method. In SAPPA, time zones that show stationary temporal behavior in the major rSVs are identified, and the experimental data at those identified stationary time zones are used as the basis to fit the experimental data at each time delay. The number of necessary time zones is the same as the number of the main components in the time range of

interest, that is, three in the time range from 100 ps to 10 μ s. Inspection of the first three rSVs multiplied by corresponding singular values (Fig. 2c) shows that the time zones around 100 ps, 10 ns, and 10 μ s satisfy the stationary condition (that is, the rSVs do not change much with time). Then we used the experimental difference curves corresponding to these three time zones (more specifically, the difference curves at 100 ps, 10 ns, and 10 μ s) to fit the corresponding contribution at each time delay. The obtained profiles are shown in Fig. S15a. These profiles already show the general kinetic framework containing A \rightarrow B \rightarrow C. At this point, it is worth noting that three, the number of main components for the second time range from 100 ps to 56.2 ns, is compatible with the parallel kinetic framework containing both A \rightarrow B and A \rightarrow C as well as the sequential one containing A \rightarrow B \rightarrow C. The SAPPA kinetic profiles rule out the parallel framework. For this reason, we showed only those with the sequential one in Fig. S14 (to avoid unnecessary complexity that may confuse readers).

While this simple framework of A \rightarrow B \rightarrow C needs only two time constants, three time constants obtained from rSVs (4.6 ns, 47 ns, 588 ns) indicate that there should be one more kinetic process involved. Fitting these profiles using these time constants show the most natural scenario is that 4.6 ns accounts for A \rightarrow B and both 47 ns and 588 ns account for B \rightarrow C, meaning that a B-to-C biphasic transition (model (6) in Fig. S14). Moreover, a comparison of the SAPPA kinetic profiles (Fig. S15b) and the expected kinetic profiles of the nine candidate frameworks (Fig. S15c) immediately allows for ruling out models (1) ~ (5), (8), and (9), whereas those of models (6) and (7) are compatible with the SAPPA profiles. Among these two models, only model (6) contains the biphasic transition from the second intermediate to the third intermediate, which is one of the common features observed in WT and all other mutants (F97Y, T72V, and I114F) studied by TRXSS. In other words, if A, B, and C are assigned to I₁, I₂, and I₃, respectively, model (6) is the same as the kinetic framework of WT, F97Y, T72V, and I114F. It should be noted that the I₂-to-I₃ biphasic transition originates from the existence of both fully photolyzed and partially photolyzed forms. The fully photolyzed form converts faster than the partially photolyzed form due to the allosteric effect. One cannot rule out the possibility of model (7), but we consider this model highly unlikely because it is difficult to find any reason justifying why only the dimer of K30D shows such a drastically different kinetic framework.”

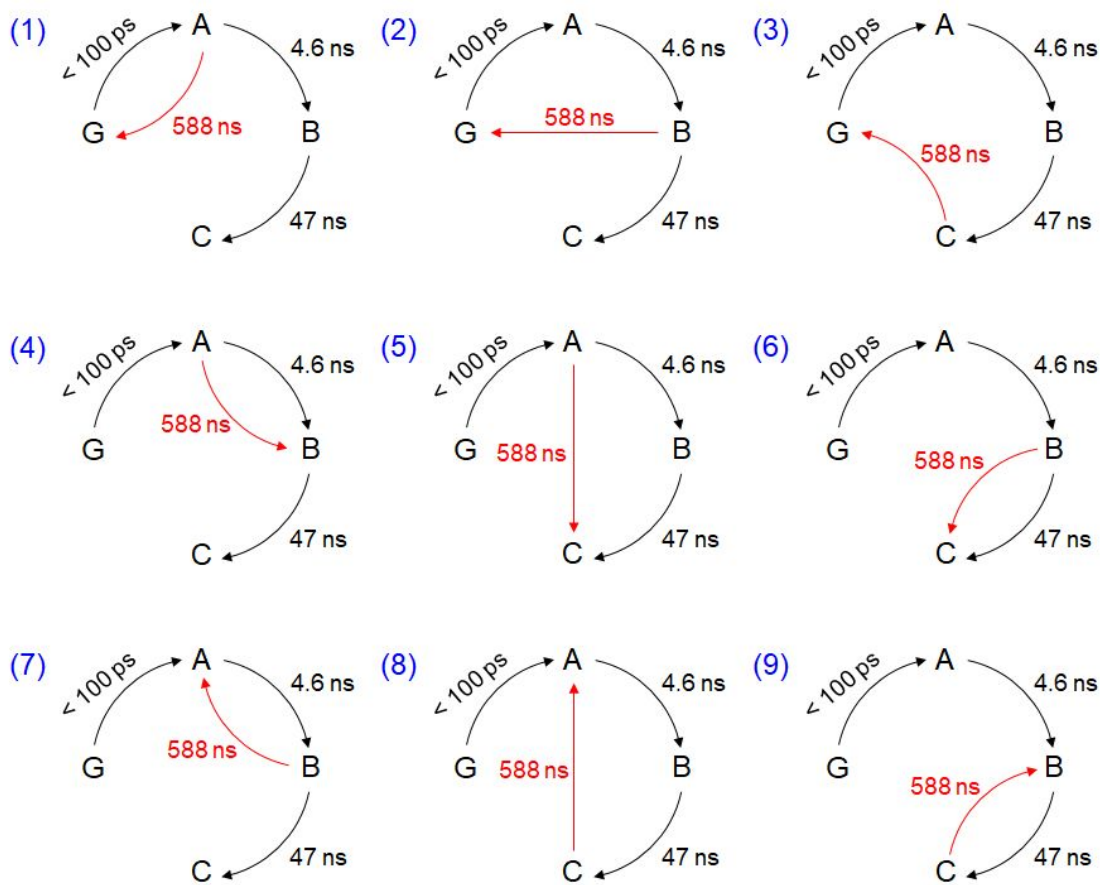


Fig. S14. All possible candidate kinetic models for the time range from 100 ps to 10 μ s, containing the sequential kinetic framework of $G \rightarrow A \rightarrow B \rightarrow C$ indicated by black arrows, where G, A, B, and C refer to the ground state, the first intermediate, the second intermediate, and the third intermediate, respectively. In all kinetic models, time constants of 4.6 ns and 47 ns are commonly assigned to $A \rightarrow B$ and $B \rightarrow C$ transitions, respectively, to be compatible with the results of SVD analyses in the reduced time ranges shown in Fig. S10. The kinetic models (1) ~ (9) are distinguished from each other in terms of the assignment of the time constant of 588 ns. In each kinetic model, the assignment of 588 ns is indicated by a red arrow.

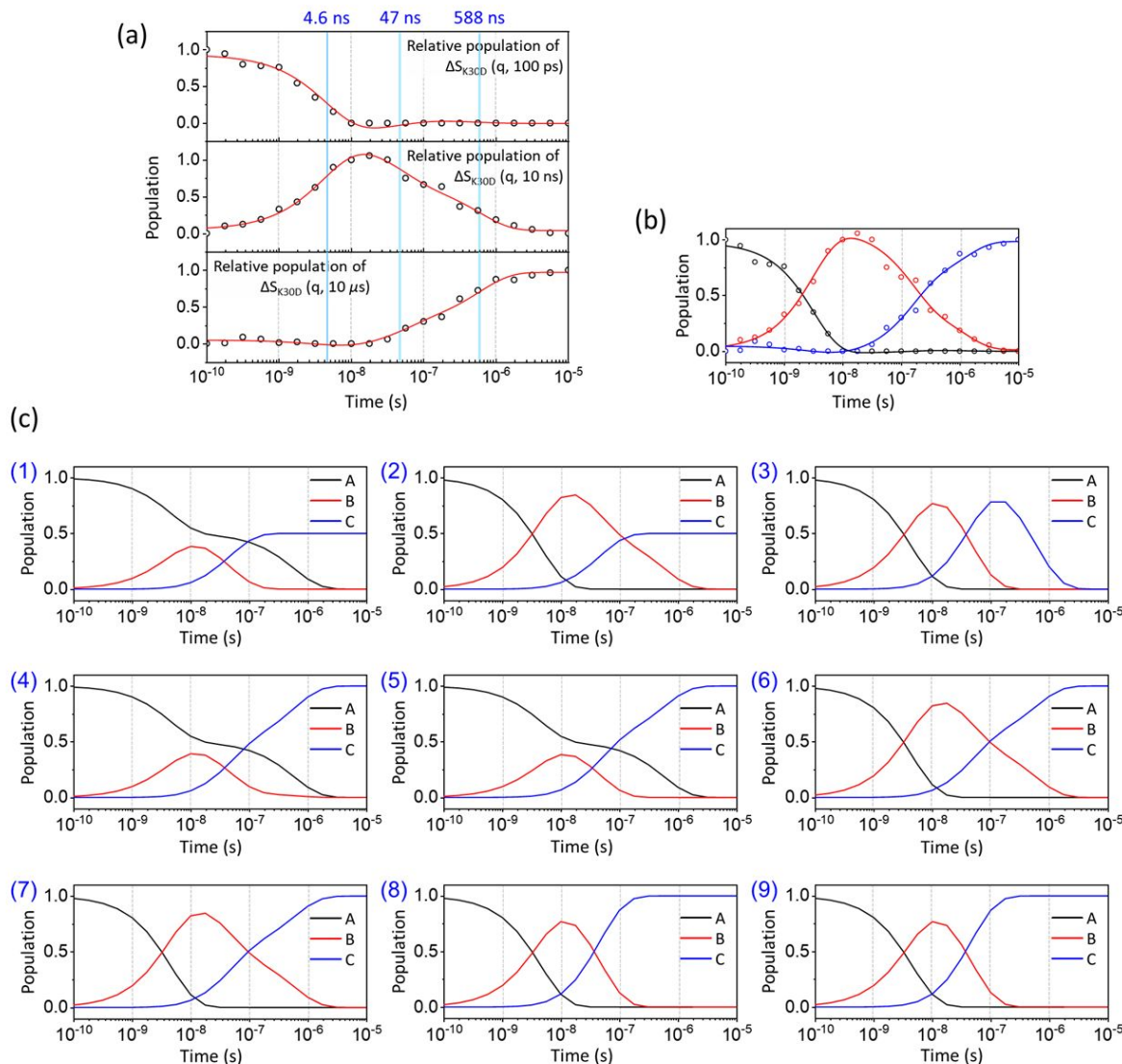


Fig. S15. (a) The SAPPA kinetic profiles obtained from SAPPA using the experimental difference curves at 100 ps, 10 ns, and 10 μs as the basis spectra to fit the relative contributions of the three basis spectra as a function of time. The relative populations indicated in empty circles are obtained from SAPPA, and the red curves are from fitting the three SAPPA kinetic profiles with the common time constants fixed at those obtained from the fit of rSVs (4.6 ns, 47 ns, 588 ns). (b) The SAPPA kinetic profiles of (a) shown in a different style to facilitate easy comparison with the kinetic profiles from candidate kinetic models of (c). The profiles of the first, second, and third basis components are shown in black, red, and blue, respectively. (c) The simulated kinetic profiles of three intermediates for the nine candidate kinetic models shown in Fig. S14. Comparison of the kinetic profiles in (c) and the SAPPA kinetic profiles in

(b) show that only models (6) and (7) are compatible with the experimental data, ruling out the other models.

Despite the complications in providing a definitive interpretation of the data, I think that this manuscript is interesting, provides useful information, and merits publication. The data presented are of high quality, the authors are forthcoming about ambiguities in their modeling, and interesting analytical techniques are used that can serve as an example to others studying multimeric complexes by X-ray solution scattering. More broadly, the field of time-resolved structural biology needs more studies that demonstrate the use of specific mutants to sort out functional and non-functional motions, and to dissect the relevant dynamics, and this is an excellent example using a mutation that abolishes a key salt bridge that contributes to allosteric communication networks. I do wonder though why the authors didn't choose a more conservative mutation, such as K30A, that would have broken the salt bridge without introducing unnecessary electrostatic repulsion that certainly influences the monomer-dimer equilibrium?

→ We thank the reviewer for positively evaluating our work and acknowledging the related importance. We chose K30D to elucidate the effect of the salt bridge because K30D had been previously studied with other methods, providing clues that can be used in the kinetic modeling process and the ground that the results of the structural dynamics obtained using our TRXSS data can be compared with. As the reviewer mentioned, a mutant such as K30A may have the effect of abolishing salt bridges without a significant effect on the monomer-dimer equilibrium, but there was no reference on K30A, having made us reluctant to select such a mutant for our study.

I suggest that, prior to publication, the authors make minor revisions to the conclusions to include more interpretation of their results in a way that connects the K30-D89 salt bridge to the structural transitions modeled from their K30D data and describe for the WT based on previous work. For example, it is counterintuitive to me that in the WT, which maintains the salt bridge, there is more intersubunit motion than for the mutant, which loses the interaction and yet appears to be a more rigid dimer.

→ We appreciate the reviewer's insightful suggestion. As the reviewer pointed out, it may be surprising and even counter-intuitive to readers that K30D, which lost salt bridges and has smaller intersubunit motion (such as larger heme-heme distance contraction and intersubunit

rotation) than WT, may appear more rigid than WT in this sense. Considering the reviewer's comment, we added the following discussion to the revised conclusion.

"These comparisons of the structural dynamics and kinetics of K30D and WT offer insights into the role of salt bridges. If interfacial salt bridges serve only as structural constraints to increase the rigidity between two subunits, one may expect that K30D, where the salt bridges are abolished, would have a more flexible intersubunit motion than WT. The data show the opposite; K30D has a suppressed intersubunit motion, suggesting a more sophisticated role of interfacial salt bridges beyond a simple structural glue between subunits. It should be noted that the structural changes of HbI are closely related to allosteric regulation. Once a ligand is attached to the heme of one subunit, this even causes the change of the ligand-binding affinity of the other subunit via allosteric regulation. This consideration renders that the interfacial salt bridges not only assist the physical connection of two subunits but also play a critical role in the global structural signal transduction of one subunit to the other subunit via a series of well-organized structural transitions."

Effect of Abolition of Intersubunit Salt Bridges on Allosteric Protein Structural Dynamics

Minseo Choi,^{a,b,‡} Jong Goo Kim,^{b,‡} Srinivasan Muniyappan,^{b,‡} Hanui Kim,^{a,b} Tae Wu Kim,^b Yunbeom Lee,^{a,b} Sang Jin Lee,^{a,b} Seong Ok Kim,^b and Hyotcherl Ihee^{*,a,b}

^a*Department of Chemistry and KI for the BioCentury, Korea Advanced Institute of Science and Technology (KAIST), Daejeon 34141, Republic of Korea*

^b*Center for Nanomaterials and Chemical Reactions, Institute for Basic Science (IBS), Daejeon 34141, Republic of Korea*

*Corresponding author. Email: hyotcherl.ihee@kaist.ac.kr

‡These authors contributed equally to this work.

†Electronic Supplementary Information (ESI) available: See DOI: 10.1039/x0xx00000x

Abstract

Salt bridge, one of the representative structural factors established by non-covalent interactions, plays a crucial role in stabilizing the structure and regulating the protein function, but its role in dynamic processes has been elusive. Here, to scrutinize the structural and functional roles of the salt bridge in the process of performing the protein function, we investigated the effects of salt bridges on the allosteric structural transition of homodimeric hemoglobin (HbI) ~~from *Seaphareca inaequivalvis*~~ by applying time-resolved x-ray solution scattering (TRXSS) to the K30D mutant, in which the interfacial salt bridges of wild type (WT) are abolished. The TRXSS data of K30D is consistent with the kinetic model that requires one monomer intermediate in addition to three structurally distinct dimer intermediates (I_1 , I_2 , and I_3) observed in WT and other mutants. The kinetic and structural analyses show that K30D has an accelerated biphasic transition from I_2 to I_3 ~~compared to WT~~ by more than nine times compared to WT and lacks significant structural changes in the transition from R-like I_2 to T-like I_3 observed in WT, unveiling that the loss of the salt bridges interrupts R-T allosteric transition of HbI. ~~Consequently, I_3 of K30D has a structure more similar to the ground state compared to I_3 in WT and other mutants. Nevertheless~~Besides, the correlation between the bimolecular CO recombination rates in K30D, WT, and other mutants, reveals that the bimolecular CO recombination is abnormally decelerated in K30D, indicating that the salt bridges also affect the cooperative ligand binding in HbI. These comparisons of the structural dynamics and kinetics of K30D and WT render that the interfacial salt bridges not only assist the physical connection of two subunits but also play a critical role in the global structural signal transduction of one subunit to the other subunit via a series of well-organized structural transitions.

Introduction

A function of a protein has an intimate connection with its three-dimensional structure. Thus, understanding the interactions inside the protein that affects the structure provides key clues for uncovering the function of a biological system. The structure of a protein is determined by the covalent interactions between amino acid residues to establish the backbone of the protein as well as the non-covalent interactions such as hydrogen bonds, van der Waals interactions, ionic interactions, and hydrophobic interactions that determine how the protein folds. The salt bridge is one of the typical structural factors generated by non-covalent interactions found in many proteins and is formed by a combination of hydrogen bonds and ionic interactions. In a protein, a salt bridge is mainly constructed between a negatively charged carboxylate of aspartic acids or glutamic acids and cationic ammonium of lysines or guanidiniums. Many studies have been conducted to unveil the structural and functional roles of salt bridges in proteins. The ~~role of the~~ salt bridge in the structural aspect mainly plays a role in stabilizing entropically unfavorable conformations, enhancing the stabilities of secondary, tertiary, and quaternary structures, and having resistance to protein aggregation.^{1, 2} Since the salt bridge contributes to stabilizing the protein structure, the protein's activity is inevitably regulated by the salt bridge. Many cases have been reported that the proteins cannot perform their original functions when the salt bridges are abolished.²⁻⁴ Although much research has been conducted on ~~the~~ salt bridges due to their importance in determining the structures and functions, most studies have been conducted only on static equilibrium states. In reality, however, performing a protein function is not a static process in which the protein stays in a specific structure but a dynamic process in which the structure changes over time. Therefore, it is important to identify how the salt bridge affects the structural dynamics of a protein, for example, the structures of reaction intermediates and the associated reaction rates.

In this ~~work~~regard, here we investigated how the structural dynamics of a protein are altered with the presence or absence of salt bridges to improve the understanding of the structural and functional role of the salt bridges in the ~~middle~~course of the dynamic biological process. Specifically, we investigated the role of the salt bridges during the allosteric structural transition of homodimeric hemoglobin (HbI) from *Scapharca inaequivalvis*. ~~The~~ allostericAllotropie regulation is one of the essential mechanisms regulating the function of proteins, by which the structural change at one site leads to significant feedback at a remote site of the same macromolecular entity. A well-known example is human tetrameric hemoglobin (Hb), where the binding of dioxygen or carbon monoxide is known to benefit from

allosteric regulation.⁵⁻¹² While the tetrameric structure of Hb makes detailed experimental studies difficult,¹³ HbI offers a greatly simplified model system thanks to its homodimeric structure. Despite being only a dimer, the characteristics of cooperative ligand binding and allosteric structural transitions are clearly expressed between the liganded R state with high ligand affinity and the unliganded T state with low ligand affinity.¹⁴⁻²⁵²⁶

HbI has two symmetrically linked salt bridges between Lys30 and Asp89 at the subunit interface. The salt bridges are one of the essential factors composing the intersubunit network and stabilizing the dimeric assemblage with two subunits connected. By two symmetrically linked intersubunit salt bridges between Lys30 in one subunit and Asp89 in the other subunit, one subunit may communicate to the other subunit. The K30D mutation, where the Lys30 residues of the two subunits consisting of the salt bridges of the wild type (WT) are replaced with Asp30 residues, abolishes the only salt bridges at the subunit interface by introducing charge repulsion between Asp30 and Asp89 (Fig. 1) so that this mutant is a relevant system for identifying the effect of the salt bridges on the structural dynamics of HbI.

A study using spectroscopic characterization on K30D reported the dimerization constants about unliganded and liganded derivatives, the oxygen equilibrium measurements, and the kinetics of oxygen release.²⁶²⁷ It was reported that the cleavage of the salt bridges destabilizes the intersubunit network and dimeric assemblage of HbI, resulting in a change of the mechanism of cooperativity.²⁶²⁷ According to the reported dimerization constant,²⁶²⁷ whereas WT mostly exists as the dimeric form in nature, the fraction of the monomer is not negligible in K30D due to the weakened interaction in the interface. The local structural changes near the heme pocket and the kinetics upon oxygen release in K30D were investigated by spectroscopic studies and equilibrium oxygen-binding experiments.²⁶²⁷ Still, more detailed kinetic and structural information, such as lifetimes and tertiary and quaternary structures of reaction intermediates, are unclear. In this regard, time-resolved x-ray solution scattering (TRXSS),²⁷⁻³²²⁸⁻³³ can provide complementary dynamic information on the allosteric structural transition of K30D in solution for unveiling the effect of the salt bridges in HbI on the structural dynamics. TRXSS, also known as time-resolved x-ray liquidography (TRXL), is a useful technique that offers complimentary advantages over conventional methods, as it allows for easy observation of the structural dynamics of proteins in physiological environments.

In this work, to elucidate how the interfacial salt bridges play a role in the allosteric structural transition in HbI, we performed the TRXSS experiment on the K30D in solution and extracted the structures of the intermediates and determined kinetic parameters based on the

modified kinetic model that considered the monomer fraction. In particular, we obtained the detailed structural parameters in the intermediates of K30D HbI, such as root-mean-square deviations (RMSDs), displacement plots, subunit rotation angles, heme-heme distances, and distances between C α atoms of the key residues involved in the salt bridges in WT HbI, and quantitatively compared these structural parameters with those of WT HbI. We found that all the three dimer intermediates (I_1 , I_2 , and I_3) of K30D have R-like structures, unlike WT involving a transition from R-like I_1 and I_2 to T-like I_3 . These observations indicate that the dramatic structural change associated with the R-T transition is remarkably suppressed by losing the salt bridges in K30D. Considering that the bimolecular CO recombination is decelerated in K30D although I_3 of K30D has the structure more similar to the ground state compared to WT, the loss of the salt bridges may diminish the ligand-binding affinity and eventually make the CO recombination process slow.

Experimental

Sample preparation

The K30D mutation was introduced into the native recombinant HbI plasmid using the EZchange™ Site-directed Mutagenesis Kit (Enzyomics) with the following oligonucleotides encoding K30D mutation: 5'-GGTCGGACAAAGATGGTAACGG-3' and 5'-CCGTTACCATCTTGTCCGAACC (Genotech). The K30D mutant (K30D) was over-expressed in *E. coli* and purified according to the method³³ described for the wild type (WT)-*coli* and purified according to the method³⁴ described for WT. Carbonmonoxy derivatives of K30D solution for the photodissociation reaction were prepared as follows. A 2–4 mM deoxy K30D solution in 100 mM phosphate buffer (pH 7) was prepared in a rubber-topped air-tight vial. The protein concentration was determined from the absorbance at 578 nm using the absorption coefficient of heme-oxygenated derivatives ($14.3 \text{ mM}^{-1} \text{ cm}^{-1}$). The deoxy K30D was reduced by adding 10 μL of 1 M sodium dithionite solution under a nitrogen atmosphere. The reduced samples were exposed to CO gas for 30 minutes to convert deoxy to the CO-bound K30D. The sample solution was prepared just before the x-ray solution scattering measurement. An aliquot of the resulting CO-bound K30D-HbI(CO)₂ solution was transferred into a quartz capillary with a 1 mm diameter (Hampton Research) and immediately sealed with epoxy to minimize gas exchange while CO gas was purged continuously into the capillary.

Data acquisition

The time resolved x-ray solution scattering experiment of K30D was conducted at the 14IDB BioCARS beamline at Advanced Photon Source using the experimental setup of a typical pump-probe method. Circularly polarized laser pulses generated from a picosecond laser system were sent to an optical parametric amplifier (TOPAS) to generate output pulses with the center wavelength of 532 nm and the temporal duration of ~35 ps. The laser light was focused on $0.15 \times 0.60 \text{ mm}^2$ at the sample position and finally had an energy density of 1 mJ/mm². The x-ray pulse peaked at 12 keV with a long wavelength tail of ~4% and the photon flux of $\sim 10^9$ photons/pulse. The size of the x-ray beam was adjusted to be $0.9009 \times 0.7007 \text{ mm}^2$ at the sample, which ~~is was~~ smaller than the laser spot size, to minimize the timing jitter caused by the spatial error between laser and x-ray pulses. After a laser pulse passed through the sample to induce the reaction, an x-ray pulse arrived with a time delay, Δt , and time-resolved x-ray scattering data were measured at time delays in the range from 100 ps to 10 ms. The helium cone was utilized to reduce the air scattering by x-ray. Two-dimensional (2D) scattering patterns were collected using an area detector (MarCCD) located at a distance of 185 mm from the sample position. The capillary containing the protein sample was moved along the axis perpendicular to the pulse train of x-ray and laser and was set to perform repetitive motion in the forward and backward directions to provide a fresh sample for each x-ray and laser pair. The obtained 2D x-ray scattering patterns have centrosymmetry due to the random orientation of the molecules in the solution phase, so that one-dimensional (1D) x-ray scattering curves can be obtained by azimuthally integrated as a function of the magnitude of the momentum transfer vector, $q = (4\pi/\lambda)\sin(2\theta/2)$ where λ is the x-ray wavelength and 2θ is the scattering angle. The 1D x-ray scattering curves, $S(q, \Delta t)$, contain information about the x-ray scattering occurring from the solvent pairs, solute pairs, and solvent-solute pairs at the corresponding time delay. The x-ray scattering signal from the solvent molecule ~~is was~~ much larger than the signal of our interest resulting from the reaction of the solute molecules. The scattering curve at the negative time delay, $-5 \mu\text{s}$, containing the signal from the unreacted sample solution was subtracted from the scattering curve for each time delay, and the scattering signal generated by the bulk solvent was removed by this process. As a result, we obtained the time-resolved difference x-ray solution scattering curves, $\Delta S(q, \Delta t)$. The time delays used in the experiments are as follows.

—5 μ s, 100 ps, 178 ps, 316 ps, 562 ps, 1 ns, 1.78 ns, 3.16 ns, 5.62 ns, 10 ns, 17.8 ns, 31.6 ns, 56.2 ns, 100 ns, 178 ns, 316 ns, 562 ns, 1 μ s, 1.78 μ s, 3.16 μ s, 5.62 μ s, 10 μ s, 17.8 μ s, 31.6 μ s, 56.2 μ s, 100 μ s, 178 μ s, 316 μ s, 562 μ s, 1 ms, 1.78 ms, 3.16 ms, 5.62 ms, and 10 ms.

The measured x-ray ~~solution~~-difference scattering curves ~~contain~~contained the signal from the thermal heating of the solvent. For the data analysis, we removed the thermal heating contribution using a well-established method.³⁴⁻³⁷³⁵⁻³⁸ During the experiment, the temperature was maintained at ~~2025~~ °C by a stream of cold nitrogen gas (Oxford Cryostream).

Results and discussion

Kinetic analysis of time-resolved difference solution scattering curves

Time-resolved difference x-ray solution scattering curves, $\Delta S(q, t)$, obtained for time delays (t) from 100 ps to 10 ms are shown in Fig. 2a. The data exhibit oscillatory features along the q -axis due to protein structural changes. To extract kinetics information of intermediates and their structures from $\Delta S(q, t)$, we followed the well-established procedure³⁴⁻³⁷³⁵⁻³⁸ which had been applied to previous TRXSS studies on WT and various mutants of HbI, consisting of kinetic analysis using singular value decomposition (SVD) and principal component analysis (PCA). As detailed in the electronic supporting information (ESI), SVD and the global fit of left singular vectors (lSVs) show that the kinetics involves four structurally distinct intermediates and five time constants of 4.6 (± 0.7) ns, 47 (± 13) ns, 588 (± 81) ns, 616 (± 108) μ s, and 5.34 (± 5.22) ms. The kinetics of all the HbI proteins so far studied with TRXSS, including WT, F97Y,³⁶³⁷ T72V,³⁵³⁶ and I114F³⁴³⁵ can be explained with the same kinetic framework with only minor variations. This framework has three intermediates, a transition from the first intermediate to the second intermediate ($I_1 \rightarrow I_2$), a biphasic transition from the second intermediate to the third intermediate ($I_2 \rightarrow I_3$), and bimolecular recombination to recover CO-bound HbI(CO)₂. Compared to the WT data, which exhibits three intermediates and seven time constants, K30D has one additional intermediate and a smaller number of kinetic components, requiring a more significant alteration to the known kinetic framework.

To establish the kinetic framework (Fig. 3a), ~~we tried to obtain clues about the number of intermediates associated with each of the relaxation times by performing SVD analyses for various reduced time ranges³⁸ in addition to the whole data. As detailed in the SI, such analyses reveal that the first time constant of 4.61 ns can be attributed to the transition from I_1 to I_2 , and the two time constants of 46.6 ns and 588 ns need to be assigned to the biphasic transition from I_2 to I_3 . As a result, among five time constants, two (616 μ s and 5.34 ms) remain to be assigned,~~

~~and the identity of one intermediate among four remains to be determined.^{3a)}, we used two effective methods that can greatly facilitate narrowing down the kinetic models compatible with the experimental data: (i) the numbers of species from the SVD results on various reduced time ranges³⁹ in addition to the whole data and (ii) SVD-aided pseudo PCA analysis (SAPPA).³⁹ As detailed in the SI, such analyses reveal that the first time constant of 4.6 ns can be attributed to the transition from I₁ to I₂, and the two time constants of 47 ns and 588 ns need to be assigned to the biphasic transition from I₂ to I₃. As a result, among five time constants, two (616 μ s and 5.34 ms) remain to be assigned, and the identity of one intermediate among four remains to be determined.~~

We considered the possibility that this remaining intermediate is either a monomer or a dimer and built the kinetic models for both scenarios (Figs. S2a and S2b, respectively). The calculated curves from both kinetic models (Figs. S2c and S2d, respectively) gave equally satisfactory agreements with the experimental data, meaning that the fit quality alone cannot discriminate whether the fourth species is a dimer or a monomer. Nevertheless, we favor the possibility of a “monomer” intermediate for the following reasons. (i) K30D has a weakened network of interactions between Asp30 and Asp89 located in the subunit interface. K30D has a dimerization constant of 1.2×10^3 M⁻¹ at 10 °C under the equivalent condition,²⁶²⁷ and the ratio of the monomer is 41% in an aqueous solution. (ii) The monomeric unit of K30D can be regarded as a monomeric heme protein, whose photoinduced structural changes were observed in many time-resolved studies,^{27, 39-5428, 40-55} and thus it is plausible that K30D monomer undergoes the structural change induced by photoexcitation. (iii) The simulated difference scattering intensity of the monomer shows a magnitude that cannot be neglected compared to that of the dimer (As detailed in the ESI[†] and Fig. S3). This result demonstrates that if the dimer intermediates can be distinguished in the TRXSS signals, the monomer intermediate should also be distinguished. Therefore, we considered the possibility of the monomer intermediate in the kinetic model. To avoid any confusion, from now on, intermediates refer to the dimer intermediates and *i* refers to the monomer intermediate. A more detailed explanation for the process of choosing the best kinetic model is described in the ESI[†].

Finally, species-associated difference scattering curves (SADSs) and time-dependent concentrations of K30D are compared with those of WT in Fig. 3. To distinguish the intermediates for WT and K30D, we labeled I₁, I₂, and I₃ of WT as I₁^{WT}, I₂^{WT}, and I₃^{WT}, respectively, and likewise labeled the intermediates of K30D as I₁^{K30D}, I₂^{K30D}, and I₃^{K30D}, respectively. For K30D, we labeled the monomeric form of the initial state as K30D mHbI(CO)

and the dimeric form of the initial state as K30D HbI(CO)₂. According to the determined kinetic model, K30D HbI(CO)₂ is converted to the earliest intermediate, I₁^{K30D}, within the experimental time resolution (< 100 ps), and I₁^{K30D} transforms to I₂^{K30D} with a time constant of 4.6 ns, which is slightly larger than that of WT (3.2 ns), indicating that the absence of salt bridges affects the earliest intermediates although the effect is not severe. K30D shows the biphasic I₂^{K30D}-to-I₃^{K30D} transitions, as in WT and other mutants, with time constants of 47 ns and 588 ns, which are smaller than those of WT (730 ns and 5.6 μ s) by the factors of 15.5 and 9.5, respectively, indicating acceleration with respect to WT. According to TRXSS studies on WT and mutants,³⁴⁻³⁷³⁵⁻³⁸ this I₂^{WT}-to-I₃^{WT} transition accounts for the quaternary structural change where both the rotation angle and the heme-heme distance significantly change. Thus, the accelerated rates mean that either (i) these structural changes occur more rapidly, or (ii) different structural changes are involved in K30D. This result suggests that the salt bridges between the two subunits may be involved in controlling the quaternary structural change. Then, I₃^{K30D} returns to K30D HbI(CO)₂ with a bimolecular rate constant of 36 (\pm 3) mM⁻¹s⁻¹, which is nearly three times smaller than that of WT (95 mM⁻¹s⁻¹). For the monomeric form of K30D, initial K30D mHbI(CO) is converted to *i*, within the experimental time resolution (< 100 ps), and returns to K30D mHbI(CO) with a bimolecular rate constant of 309 (\pm 9) mM⁻¹s⁻¹, which is more than eight times larger than I₃^{K30D}. The fit result gives 81 (\pm 0.4) % for the fraction of monomers. The reported value at 10 °C is 41%.²⁷ The fact that the TRXSS experiment was carried out at 2025 °C can rationalize the higher monomer content. The estimated dimerization constant based on the monomer fractions at 20 °C is ~77 (\pm 1) M⁻¹.²⁶ 25 °C is ~77 (\pm 1) M⁻¹. We note that the relative portion of dimers in terms of the concentration that contributes to the difference scattering signal is ~20% (and that of monomers is ~80%), but this does not mean that the relative contribution to the difference scattering signal is 20%. One dimer contributes more strongly to the scattering signal than one monomer because a dimer is twice heavier than a monomer and a dimer generally has a larger structural change than a monomer. The relative contributions of dimers to the difference signal range from 25% to 88% depending on time, as shown in Fig. S12.

We note that the intermediates of K30D have two substrates of the fully photolyzed and partially photolyzed forms, which are structurally indistinguishable from each other. The same was revealed from previous laser power dependency studies on WT and other mutants,³⁴⁻³⁷³⁵⁻³⁸ which provided direct evidence that the partially photolyzed dimer subunit undergoes the same structural evolution as the fully photolyzed subunit, directly demonstrating the allosteric

regulation of HbI.

Structural analysis of intermediates

Structure refinement aided by Monte-Carlo simulations

The information about the 3D structures of the intermediates can be obtained via structural analysis using the SADSs for the intermediates. As shown in Fig. 3, the SADSs of WT and K30D are very different from each other for all intermediates, so it can be seen that all intermediates of K30D are structurally different from WT intermediates. In other words, the mutation from Lys30 to Asp30 changes the structure of all the intermediates. In the case of WT, F97Y and T72V mutants, the SADSs of I_1 and I_2 are not much different from each other, suggesting that the structure of I_1 and I_2 are not affected by the F97Y or T72V mutation. The SADSs of I_3 for F97Y and T72V, however, are significantly different compared to WT, indicating that the T72V and F97Y mutations alter only the structure of I_3 . To extract key structural parameters of each intermediate structure, we performed structure refinement applied with a rigid-body modeling approach using crystallographic structures as template structures, which is established in our previous study on WT.³⁴⁻³⁷³⁵⁻³⁸ In the case of K30D, since its crystallographic structures were not reported, we made the template structures for the structural analysis by modifying the crystallographic structures of WT (see the ESI[†] for details). From the structure refinement, the refined candidate structures for the intermediates were obtained, and their theoretical scattering curves show excellent agreement with the experimental SADSs (Fig. S4).

Structural analysis of the dimer intermediates of the K30D mutant: RMSDs

The key structural parameters, such as the RMSD, the displacement of the residues, the heme-heme distance, the rotation angle, and the salt bridge distance, were extracted from the candidate structures for the intermediates. To compare the overall structural differences between the intermediates of WT and K30D HbI, we calculated RMSD values in the positions of the C α atoms with respect to the reference structures (for WT, crystallographic structures of HbI(CO)₂ (PDB ID: 3SDH) and unliganded HbI (PDB ID: 4SDH) and for K30D, modified structures based on these; see the ESI[†] for details), termed as RMSD^R and RMSD^T, respectively, as shown in Figs. 4a and 4b. By comparing RMSD^R and RMSD^T values of the intermediate, it is possible to quantify allows for quantifying the degree of resembling the R-like structure or the T-like structure. In previous studies, it was found that I_1^{WT} and I_2^{WT} have

R-like structures, whereas I_3^{WT} has a T-like structure.^{34-37,35-38} Actually, I_1^{WT} (RMSD^R: $0.4 \pm 0.05 \text{ \AA}$, RMSD^T: $0.7 \pm 0.05 \text{ \AA}$) and I_2^{WT} (RMSD^R: $0.4 \pm 0.06 \text{ \AA}$, RMSD^T: $0.7 \pm 0.05 \text{ \AA}$) have larger RMSD^T than RMSD^R, whereas I_3^{WT} (RMSD^R: $0.7 \pm 0.05 \text{ \AA}$, RMSD^T: $0.4 \pm 0.04 \text{ \AA}$) has a larger RMSD^R compared to the RMSD^T, confirming that I_1^{WT} and I_2^{WT} have R-like structures and I_3^{WT} has a T-like structure. For K30D, I_1^{K30D} (RMSD^R: $0.4 \pm 0.05 \text{ \AA}$, RMSD^T: $0.8 \pm 0.06 \text{ \AA}$) and I_2^{K30D} (RMSD^R: $0.5 \pm 0.05 \text{ \AA}$, RMSD^T: $0.8 \pm 0.06 \text{ \AA}$) exhibit larger RMSD^T than RMSD^R, as in WT, indicating that I_1^{K30D} and I_2^{K30D} have R-like structures. However, the opposite trend was observed between I_3^{WT} and I_3^{K30D} . I_3^{K30D} (RMSD^R: $0.3 \pm 0.05 \text{ \AA}$, RMSD^T: $0.7 \pm 0.05 \text{ \AA}$) has a larger RMSD^T than RMSD^R, indicating that I_3^{K30D} has an R-like structure, unlike the T-like I_3^{WT} . The fact that all the intermediates of K30D have R-like structures suggests that abolishing the salt bridges in K30D restricts the efficient R-T transition in HbI.

Tertiary structural changes: displacement plots

To identify the detailed tertiary structural changes, we calculated the displacement plots of the three intermediates, as shown in Fig. 4c. The displacement of the residue is defined as the difference in distance between the C α and the iron atom of the heme in the same subunit, with respect to the reference structure. The crystallographic structures of the liganded states of WT and K30D were used as the reference structures for calculating the displacement plots of WT and K30D intermediates, respectively. In I_1 and I_2 , the magnitudes and directions of the displacements in K30D are similar to those in WT. In the case of I_3 , however, the magnitudes and directions of the displacements in K30D are different from those in WT. The displacement of I_3^{K30D} is similar to those of I_1^{WT} and I_2^{WT} than that of I_3^{WT} , meaning that the tertiary structure of I_3^{K30D} has an R-like structure in contrast to I_3^{WT} having a T-like structure. These trends are also consistent with the results obtained from the comparison of the RMSD values. We note that the displacements and RMSD values of I_3^{K30D} are between those of I_2^{K30D} and K30D HbI(CO)₂, suggesting that I_3^{K30D} has a tertiary structure located between I_2^{K30D} and K30D HbI(CO)₂ structures. This consideration indicates that, unlike WT, the tertiary structure of I_3^{K30D} returns to that of K30D HbI(CO)₂ without undergoing the R-T transition occurring in the I_2^{WT} -to- I_3^{WT} transition. I_3^{WT} undergoes a rearrangement process in which the amplitude of displacement changes dramatically, whereas this process is suppressed in I_3^{K30D} . These results confirm that the internal helices as well as the interface are affected by the absence of interfacial salt bridges.

Quaternary structural changes: heme-heme distances and subunit rotation angles

To inspect detailed quaternary structural changes, we calculated the heme-heme distance and subunit rotation angle of the three intermediates, as shown in Figs. 5a and 5b. They are the key structural parameters for quantifying the quaternary structural transition since the cooperative ligand binding of HbI is modulated by the hydrogen-bonding network between two hemes and the subunit rotation. In WT, the transition from HbI(CO)₂ (heme-heme distance = 18.4 Å, subunit rotation angle = 0°) to I₁^{WT} (18.0 ± 0.2 Å, -0.1 ± 0.5 °) and I₂^{WT} (17.9 ± 0.3 Å and 0.1 ± 0.5 °) involves very small changes in the heme-heme distances and the subunit rotation angles, indicating that I₁^{WT} and I₂^{WT} have the R-like structures. The major quaternary structural changes occur in the I₂^{WT}-to-I₃^{WT} transition (16.6 ± 0.2 Å and 3.5 ± 0.6 °), indicating that I₃^{WT} has a T-like structure, unlike I₁^{WT} and I₂^{WT}. In K30D, the heme-heme distances and subunit rotation angles of both I₁^{K30D} (18.4 ± 0.3 Å and -0.4 ± 0.6 °) and I₂^{K30D} (18.6 ± 0.2 Å and 0.5 ± 0.6 °) are similar to that of the initial HbI(CO)₂ as in I₁^{WT} and I₂^{WT}. Besides, the heme-heme distance of I₃^{K30D} (17.8 ± 0.2 Å) is closer to that of HbI(CO)₂ than unliganded HbI (16.6 Å), unlike I₃^{WT}, which has the T-like structure. The subunit rotation angle of I₃^{K30D} (-0.2 ± 0.5 °), however, is even closer to that of the initial HbI(CO)₂, whereas the subunit rotation angle of I₃^{WT} is close to that of unliganded WT HbI. Therefore, the subunit rotation angle of I₃^{K30D} is much smaller than that of the T-like I₃^{WT}. The suppression of the structural rearrangement observed in I₃^{WT}, such as the contraction of heme-heme distance and the intersubunit rotation, are consistent with the results obtained by considering the RMSD values and displacement plots. The suppressed quaternary structural changes in K30D may be caused by the weakened inter-subunit interaction of K30D, suggesting the communication by salt bridges are essential elements for normal allosteric transition in HbI. This restricted R-T transition can account for the acceleration of the I₂^{K30D}-to-I₃^{K30D} transition observed in K30D since the transition in K30D does not require significant quaternary structural changes in contrast to WT. Therefore, it takes less time for the I₂-to-I₃ transition to occur in K30D than in WT.

Distance between Cα atoms of key residues involved in the salt bridges of WT

We also inspected and averaged the distances between Cα atoms of 30th residues at the one subunit interface and 89th residues at the other subunit interface (denoted r_{30-89}). The 30th and 89th residues originally form the interfacial salt bridges in WT, but the salt bridges are abolished in K30D. We tried to identify how the movements of the helices connected by the salt bridges in WT are affected by the cleavage of the salt bridges in K30D. For this purpose,

we compared the r_{30-89} of all the intermediates for WT and K30D, as shown in Fig. 5c. I_1^{K30D} has a longer r_{30-89} (8.8 ± 0.2 Å) than I_1^{WT} (8.6 ± 0.3 Å), and also I_2^{K30D} has a longer r_{30-89} (8.7 ± 0.2 Å) than I_2^{WT} (8.5 ± 0.3 Å). The longer r_{30-89} distances in K30D than in WT indicate that the two residues are connected less tightly in K30D. The r_{30-89} values in both K30D and WT become smaller in the I_1 -to- I_2 transition, and the contraction magnitudes (~ -0.1 Å) are maintained similarly in both K30D and WT. The r_{30-89} of I_3^{K30D} (8.7 ± 0.2 Å) is smaller than that of I_2^{K30D} , whereas I_3^{WT} (9.1 ± 0.2 Å) has an increased r_{30-89} compared to I_2^{WT} . This trend is in good agreement with that the I_2^{WT} -to- I_3^{WT} transition contains a large intersubunit rotation, compared to the I_2^{K30D} -to- I_3^{K30D} transition. These results indicate that the r_{30-89} is closely linked to the interfacial salt bridges and the quaternary structural changes such as the subunit rotation angle and suggest that the interfacial salt bridges have a critical role in maintaining the proper distances between helices and having the sufficient magnitude of subunit rotation angle in the R-T transition.

Correlation between bimolecular CO recombination rate and quaternary structure of I_3

To infer the functional role of the salt bridges in cooperative ligand binding in HbI, we examined the results of the kinetic and structural analyses. Noticeably, the bimolecular CO recombination rate of I_3^{K30D} (36.1 mM $^{-1}$ s $^{-2}$) is slower than that of I_3^{WT} (95 mM $^{-1}$ s $^{-2}$), although I_3^{K30D} has an R-like structure. Intuitively, since I_3^{K30D} has a structure ~~much~~highly similar to the ground state, the recovery process of I_3^{K30D} is expected to be faster than that of I_3^{WT} . In fact, in the case of F97Y and T72V mutants, ~~of which~~whose structural dynamics were investigated using the TRXSS technique, the more are the quaternary structures of I_3 similar to the ground state, the faster are the acceleration of the bimolecular CO recombination process.^{35,36,37} for various mutants, we represented the heme-heme distances and subunit rotation angles of I_3 of WT, K30D, F97Y, and T72V in Fig. 6. For F97Y and T72V, the subunit rotation was not significantly affected, but the heme-heme contraction in F97Y and T72V was suppressed compared to WT, which is consistent with the fact that the bimolecular CO recombination rates of I_3^{F97Y} and I_3^{T72V} (1300 mM $^{-1}$ s $^{-2}$ and 310 mM $^{-1}$ s $^{-2}$, respectively) are faster than that of I_3^{WT} . In K30D, however, both the heme-heme contraction and subunit rotation are limited during the R-T transition, but the bimolecular CO recombination of I_3^{K30D} is slower than that of I_3^{WT} , unlike in F97Y and T72V. Considering that the bimolecular CO recombination process requires both the structural recovery and ligand binding, the distinct correlation in K30D may indicate that the loss of the salt bridges degrades the cooperative ligand binding affinity of K30D.

Conversely, it can be considered that the salt bridges in HbI may play a functional role in ligand binding as well as the structural role.

Structure of the monomer intermediate of the K30D mutant

Fig. S5 shows the displacement plot comparing *i* and the dimer intermediates (I_1^{K30D} , I_2^{K30D} , and I_3^{K30D}), respectively. While *i* has an R-like structure as in the K30D dimers, there are some slight differences in the movement of the CD loop, the N- and C-termini, and the F helix. The CD loop and N- and C- termini are located in the outer regions of HbI and have high flexibility in the solution. Therefore, the flexibility of these regions can lead to different structural changes between the dimer and monomer. The F helix in the monomer is exposed to the solvent, unlike in the dimer where the F helix in one subunit and the other F helix of the other subunit contact each other and form the interface.

Conclusion

In this study, we applied TRXSS to the K30D mutant of HbI to investigate the structural and functional roles of the salt bridges located at the subunit interface in the allosteric structural transition of HbI. The kinetic analysis of the TRXSS data reveals that K30D has a kinetic framework with three structurally distinct intermediates for the dimer (I_1 , I_2 , and I_3) as in WT. But, the kinetic model of K30D involves an additional intermediate (*i*) for the monomer, of which fraction dramatically increases compared to WT due to the weakened intersubunit interaction resulting from the loss of the salt bridges. A comparative study with WT reveals that the biphasic transition from I_2 to I_3 , which involves allosteric structural R-T transition in WT, is accelerated in K30D. The reason for the acceleration of the process was scrutinized by subsequent structural analysis. Structural analysis using the SADSSs of the three dimer intermediates shows that the tertiary and quaternary structural changes are suppressed in the I_2^{K30D} -to- I_3^{K30D} transition compared to WT, of which the I_2^{WT} -to- I_3^{WT} transition involves R-T structural transition with dramatic tertiary and quaternary structural changes. The structural similarity between R-like I_2^{K30D} and I_3^{K30D} can account for the acceleration of the biphasic I_2^{K30D} -to- I_3^{K30D} transition. The observations from the kinetic and structural analyses indicate that the loss of salt bridges not only leads to the weakening ~~the of~~ intersubunit interaction but also interrupts the R-T allosteric structural transition of HbI. Furthermore, the correlation between the bimolecular CO recombination rates and quaternary structures of I_3 was inspected for K30D and WT, as well as other mutants studied by TRXSS such as F97Y and T72V.

Thereby, it turned out that the bimolecular CO recombination of I₃ is abnormally decelerated in K30D, even though I₃ of K30D has ~~thea~~ structure more similar to the ground state than I₃ of WT, F97Y, and T72V. Considering that the bimolecular CO recombination process requires both the structural recovery to the ground state and the binding of CO ligands, the distinct correlation observed in K30D infers that the loss of the salt bridges degrades the ligand-binding affinity of K30D. Therefore, it can be considered that the salt bridges in HbI may play a functional role in ligand binding as well as the structural role contributing to the progression of R-T allosteric structural transition. These comparisons of the structural dynamics and kinetics of K30D and WT offer insights into the role of salt bridges. If interfacial salt bridges serve only as structural constraints to increase the rigidity between two subunits, one may expect that K30D, where the salt bridges are abolished, would have a more flexible intersubunit motion than WT. The data show the opposite; K30D has a suppressed intersubunit motion, suggesting a more sophisticated role of interfacial salt bridges beyond a simple structural glue between subunits. It should be noted that the structural changes of HbI are closely related to allosteric regulation. Once a ligand is attached to the heme of one subunit, this may trigger the change of the ligand-binding affinity of the other subunit via allosteric regulation. This consideration renders that the interfacial salt bridges not only assist the physical connection of two subunits but also play a critical role in the global structural signal transduction of one subunit to the other subunit via a series of well-organized structural transitions.

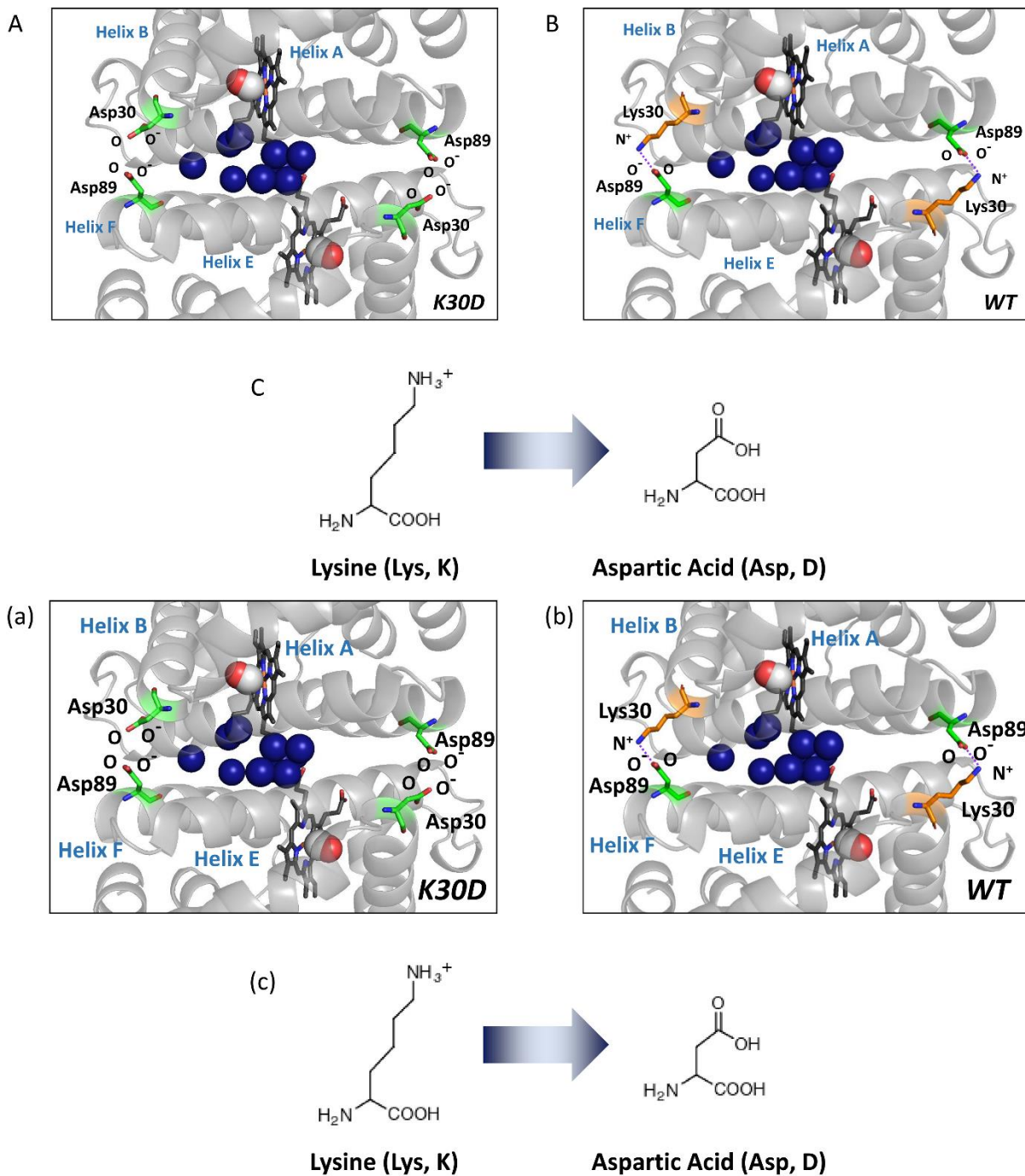


Fig. 1. Subunit interface of $\text{HbI}(\text{CO})_2$. (a) Structure of K30D $\text{HbI}(\text{CO})_2$. (b) The crystal structure of WT $\text{HbI}(\text{CO})_2$ (PDB ID: 3SDH). The structure of K30D is based on the crystal structure of WT. In K30D, the Lys30 residue (shown in orange) in each subunit of WT is replaced by Asp30 (shown in green) as shown in (c). In (a) and (b), two carbon monoxide molecules are shown with connected red and white spheres. Eleven interfacial water molecules (shown in dark blue) are well organized and connected to two subunits and hemes. In WT, the network of the subunit interface is stabilized by symmetrical salt bridges between Lys30 and Asp89. In contrast, the interface is destabilized in K30D.

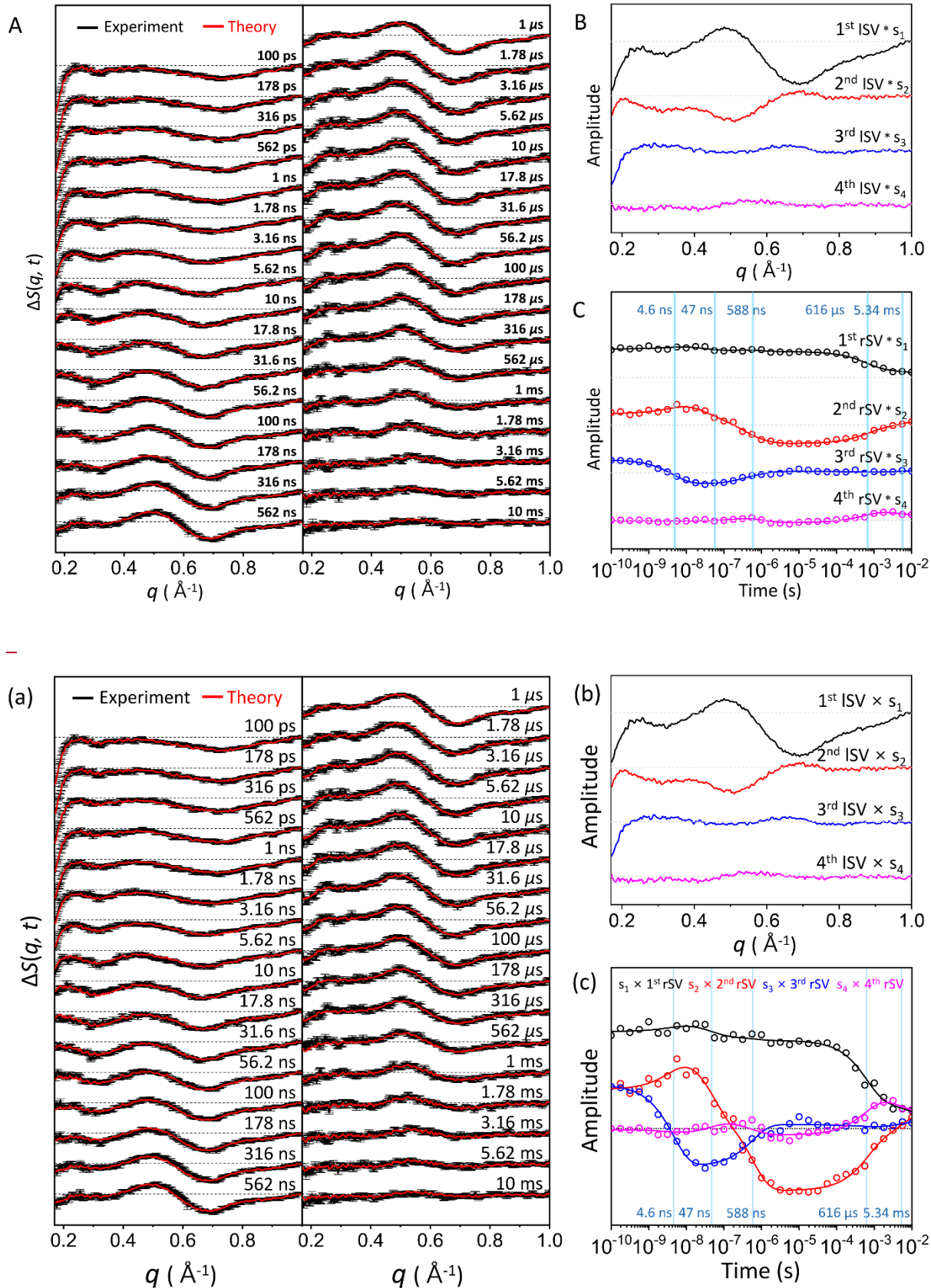
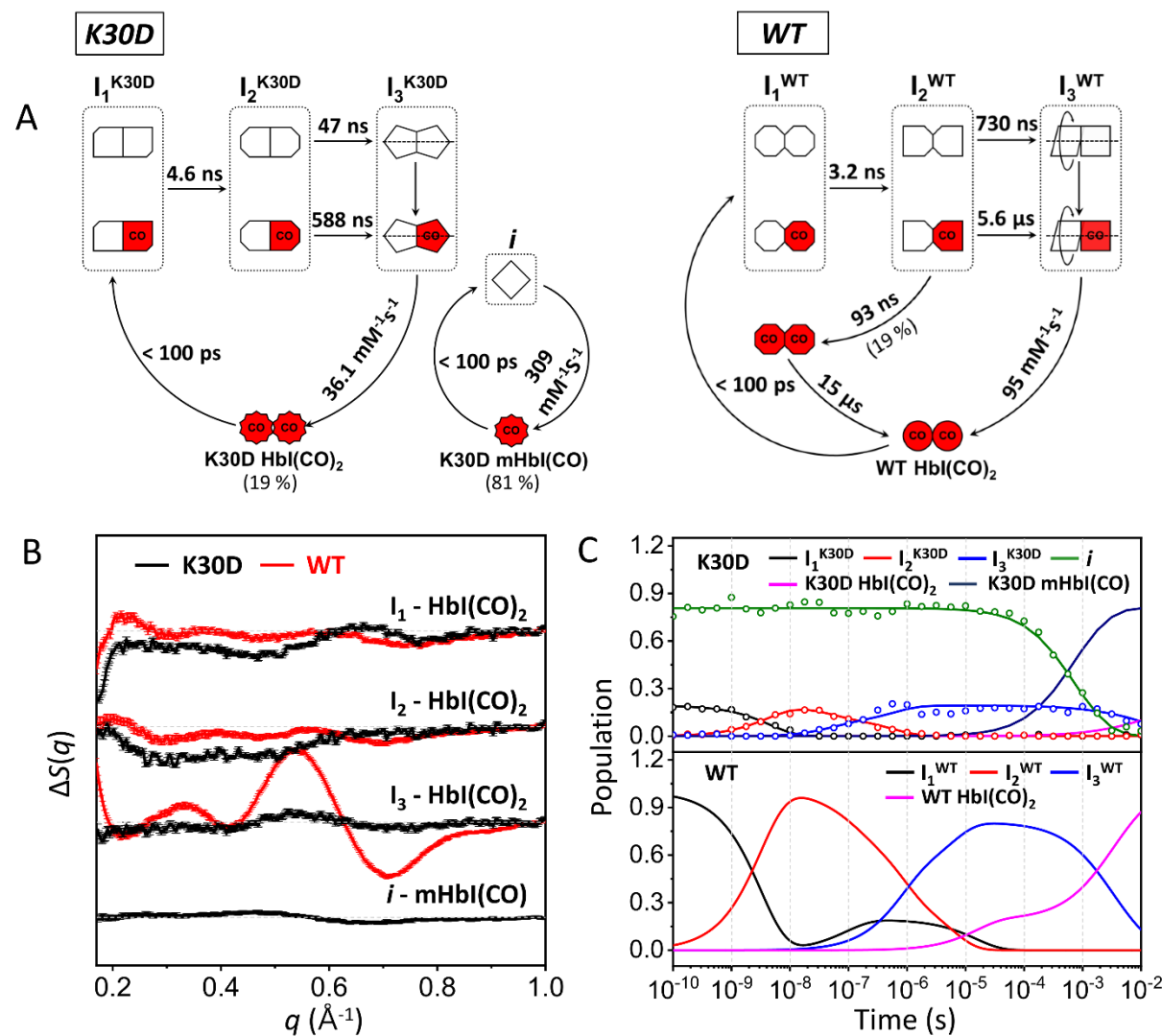


Fig. 2. (a) Time-resolved x-ray solution scattering curves, $\Delta S(q, t)$, at time delays from 100 ps to 10 ms were obtained for the K30D mutant of HbI in solution. Experimental curves with

standard deviation (shown in black) are compared with theoretical curves (shown in red) generated from a linear combination of left singular vectors (lSVs) extracted from the kinetic analysis. (b) The first four lSVs were multiplied by singular values (Fig. S1S9) from singular value decomposition (SVD) analysis. (c) The first four right singular vectors (rSVs) were multiplied by singular values and fitted by the sum of exponential functions sharing five time constants with 4.6 ns, 47 ns, 588 ns, 616 μ s, and 5.34 ms.



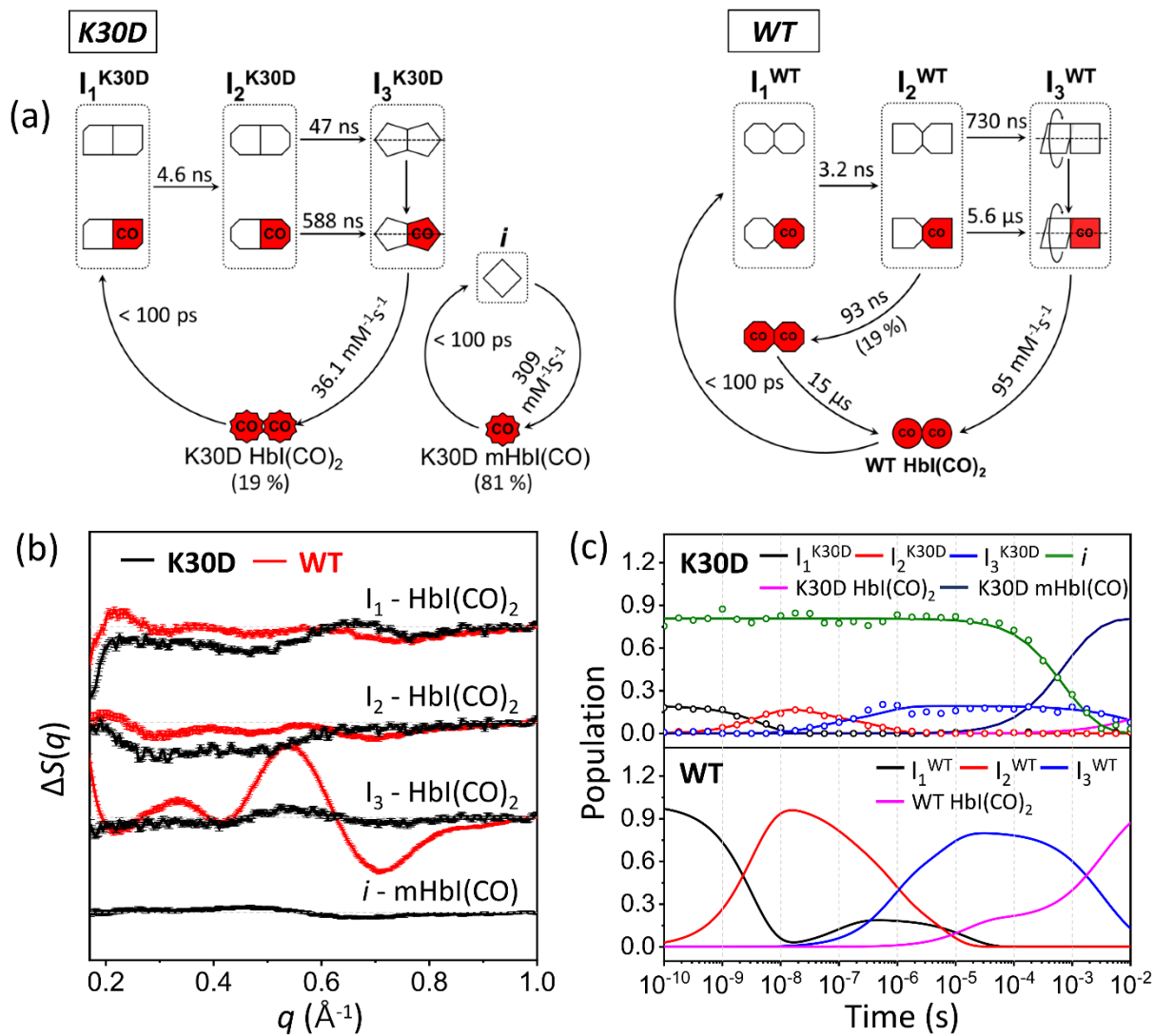


Fig. 3- (a) Kinetics models for K30D (left) and WT (right). The red (with "CO") and white symbols represent ligated and photolyzed subunits, respectively. The subunits of each intermediate are represented in different shapes to describe the change in tertiary structure change with the progress of transition from I_1 to I_2 . To indicate quaternary structure change for the transition from I_2 to I_3 , one subunit of I_3 is described as rotation with respect to the other. To indicate the photolyzed monomer, i , the diamond-shaped symbols are used. For WT, two red octagons represent a ligated form of I_1 formed by geminate recombination of CO with I_2 and is structurally indistinguishable from the photolyzed forms of I_1 . (b) Species-associated difference scattering curves (SADSs) for the intermediates of K30D (black), WT (red) HbI. (c) Population changes of the intermediates and initial $\text{HbI}(\text{CO})_2$ for K30D (upper graph) and WT (lower graph) extracted from the kinetic analysis. The open circles represent the optimized populations obtained by fitting the experimental curve at each time point with a linear combination of SADSs for the four intermediates.

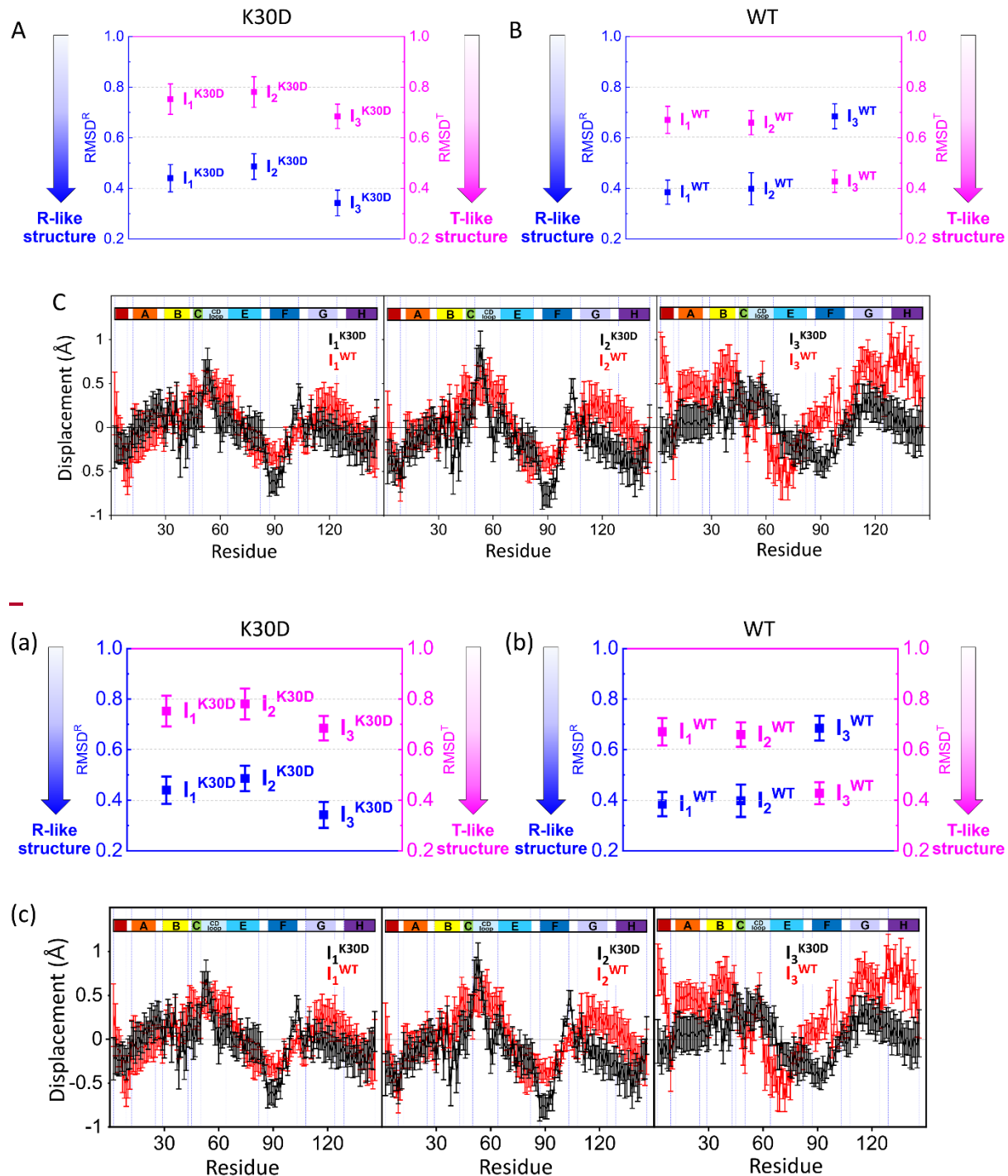


Fig. 4. Root-mean-square deviations (RMSDs) were calculated from the candidate structures of the intermediates for (a) K30D and (b) WT. As described in the main text, RMSD^{R} (blue) and RMSD^{T} (magenta) were calculated with respect to the reference structures (for WT, the crystallographic structures and for K30D, modified structures based on these; see the ESI[†] for details) of the liganded state (R state) and the unliganded state (T state), respectively. The smaller RMSD indicates the structure closer to the corresponding reference structure. The plots display that all intermediates of K30D including I_3 are close to the R-like structure rather than

the T-like structure. In contrast, in WT, only I₁ and I₂ are close to the R-like structure, while I₃ is close to the T-like structure. (c) Averaged displacement plots for K30D (black line) and WT (red line) for I₁ (left), I₂ (middle), and I₃ (right) were calculated with respect to K30D HbI(CO)₂ (mutated from 3SDH) and HbI(CO)₂ (3SDH), respectively. Error bars in (a), (b), and (c) represent standard deviation values among various candidate structures of each intermediate. K30D and WT show similar displacement patterns for I₁ and I₂ whereas they show relatively more dissimilar patterns for I₃.

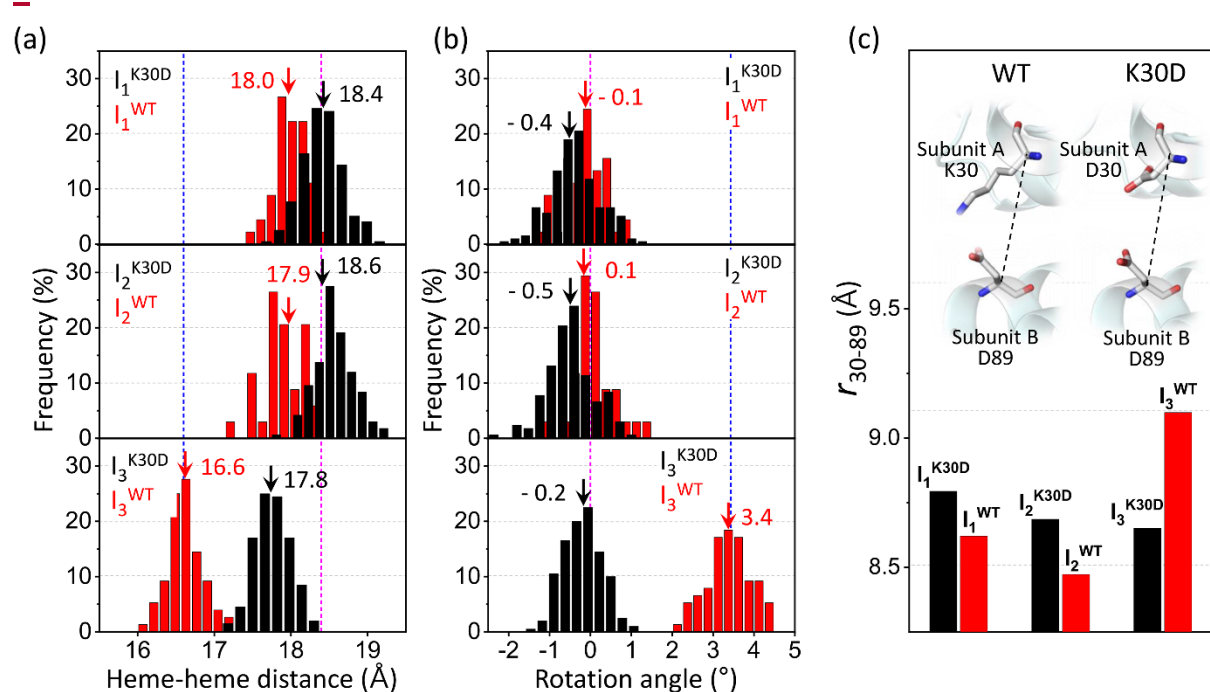
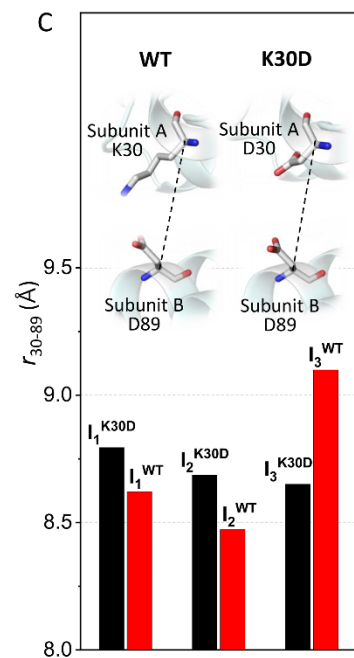
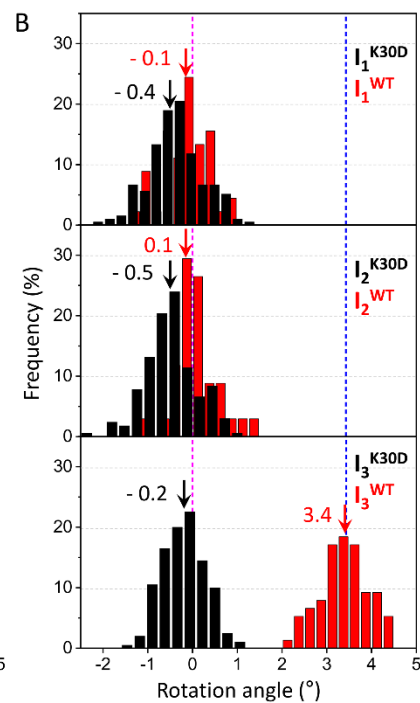
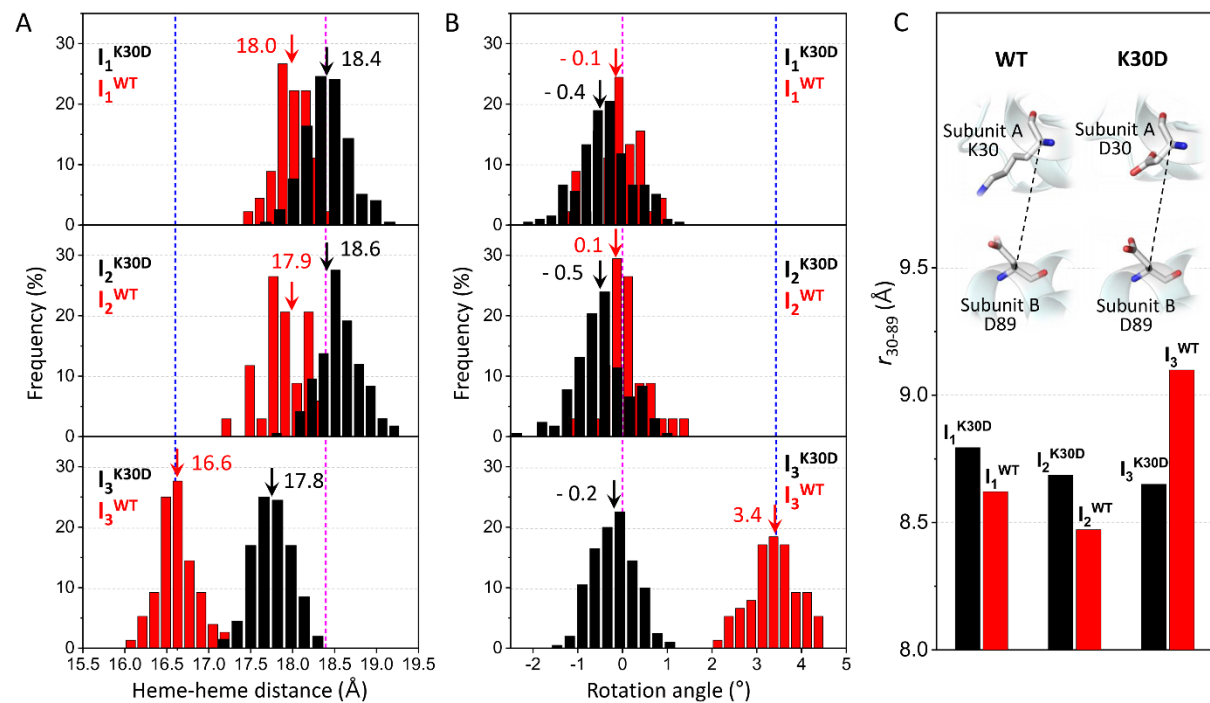


Fig. 5. Occurrence distributions of (a) the heme-heme distance and (b) the rotation angle for the intermediates for K30D (black) and WT (red). The average values for K30D and WT are indicated with downward black and red arrows, respectively, for each intermediate. For comparison, the heme-heme distances and the rotation angles of the unliganded form (PDB ID: 4SDH) and the liganded form (PDB ID: 3SDH) of WT are indicated by vertical blue and magenta dotted lines, respectively. For all three intermediates, K30D undergoes smaller changes in heme-heme distance compared to WT. In addition, the degree of rotation angles also shows that the I₃ intermediate of K30D undergoes much less rotation than that of WT. (c) The averaged distance between C α atoms in 30th and 89th residues, r_{30-89} , for K30D (black) and WT (red). The 30th and 89th residues are involved in the interfacial salt bridges in WT.

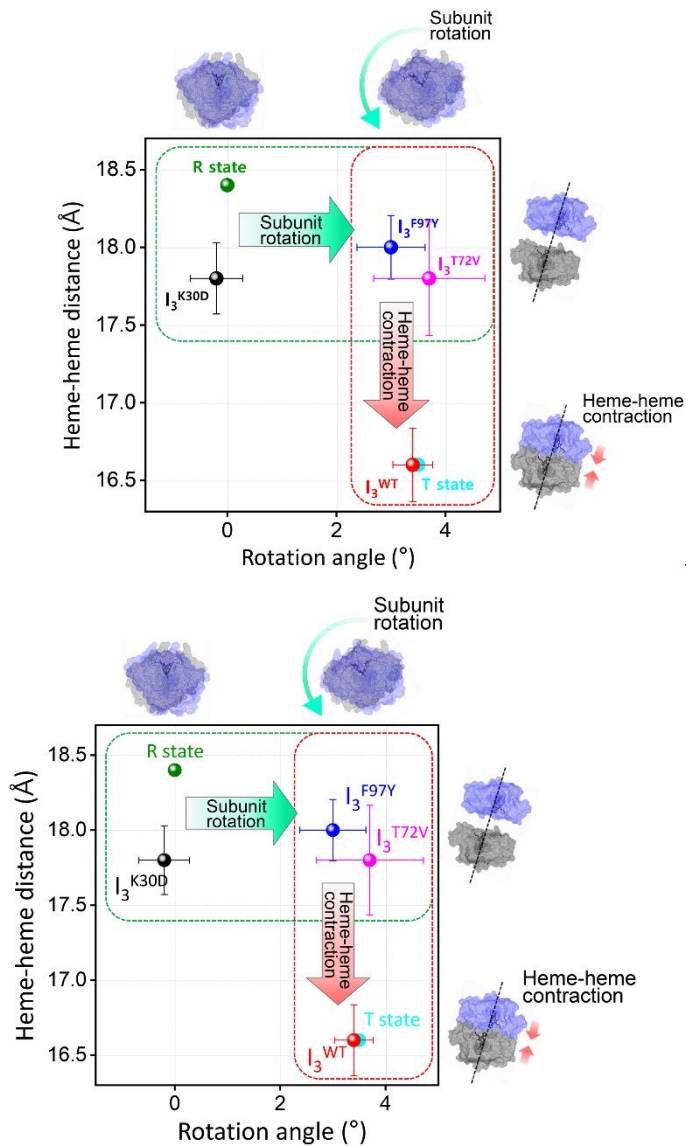


Fig. 6. Heme-heme distances of the I_3 intermediates for WT and various mutants including K30D are plotted as a function of the subunit rotation angle. For comparison, those of R and T states of WT, that is crystallographic structures of $\text{HbI}(\text{CO})_2$ and unliganded HbI , respectively, are also shown with dots in green and cyan. The dots with errors in black, red, blue, magenta correspond to averaged candidate structures of I_3^{K30D} , I_3^{WT} , I_3^{F97Y} , and I_3^{T72V} , respectively. Error bars represent standard deviation values among various candidate structures of each intermediate.

Author Contributions

H.I directed the research. H.I. designed research. S.M. performed sample preparation. T.W.K., S.L., and S.K. performed the TRXSS experiments. M.C., J.G.K., H.K., and Y.L. analyzed the data. M.C., J.G.K., and H.I wrote the paper, and all authors discussed the experimental results.

Conflicts of interest

The authors declare no competing financial interests.

Acknowledgements

This work was supported by the Institute for Basic Science (IBS-R004). We acknowledge BioCARS staff for support and helpful discussions. The use of BioCARS Sector 14 at the APS was supported by the National Institutes of Health (NIH) National Institute of General Medical Sciences Grant P41GM103543. The time-resolved setup at Sector 14 was funded in part through collaboration with P. Anfinrud (NIH/NIDDK) through the Intramural Research Program of the NIDDK. Use of the APS was supported by the U.S. Department of Energy, Basic Energy Sciences, Office of Science, under contract no. DE-AC02-06CH11357.

References

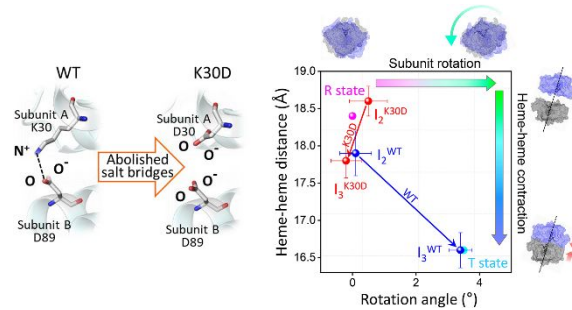
1. D. Ferrari, D. Niks, L. H. Yang, E. W. Miles and M. F. Dunn, *Biochemistry*, 2003, **42**, 7807-7818.
2. M. Ghahramani, R. Yousefi, A. Krivandin, K. Muranov, B. Kurganov and A. A. Moosavi-Movahedi, *Int. J. Biol. Macromol.*, 2020, **146**, 1142-1160.
3. J. M. Lv, J. Y. Chen, Z. P. Liu, Z. Y. Yao, Y. X. Wu, C. S. Tong and B. Cheng, *Front. Immunol.*, 2020, **11**, 583.
4. M. Al-Haggar, A. Madej-Pilarczyk, L. Kozlowski, J. M. Bujnicki, S. Yahia, D. Abdel-Hadi, A. Shams, N. Ahmad, S. Hamed and M. Puzianowska-Kuznicka, *Eur. J. Hum. Genet.*, 2012, **20**, 1134-1140.
5. M. F. Perutz, *Q. Rev. Biophys.*, 1989, **22**, 139-237.
6. S. Adachi, S. Y. Park, J. R. Tame, Y. Shiro and N. Shibayama, *Proc. Natl. Acad. Sci. U. S. A.*, 2003, **100**, 7039-7044.

7. S. Chang, M. Mizuno, H. Ishikawa and Y. Mizutani, *Phys. Chem. Chem. Phys.*, 2018, **20**, 3363-3372.
8. M. F. Perutz, *Nature*, 1970, **228**, 726-739.
9. W. A. Eaton, E. R. Henry, J. Hofrichter and A. Mozzarelli, *Nat. Struct. Biol.*, 1999, **6**, 351-358.
10. B. Shaanan, *J. Mol. Biol.*, 1983, **171**, 31-59.
11. G. Fermi, M. F. Perutz, B. Shaanan and R. Fourme, *J. Mol. Biol.*, 1984, **175**, 159-174.
12. J. Baldwin and C. Chothia, *J. Mol. Biol.*, 1979, **129**, 175-220.
13. J. Park, T. Lee and M. Lim, *Photochem. Photobiol. Sci.*, 2013, **12**, 1008-1015.
14. W. E. Royer, Jr., W. A. Hendrickson and E. Chiancone, *Science*, 1990, **249**, 518-521.
15. W. E. Royer, Jr., A. Pardanani, Q. H. Gibson, E. S. Peterson and J. M. Friedman, *Proc. Natl. Acad. Sci. U. S. A.*, 1996, **93**, 14526-14531.
16. J. E. Knapp, Q. H. Gibson, L. Cushing and W. E. Royer, Jr., *Biochemistry*, 2001, **40**, 14795-14805.
17. J. E. Knapp and W. E. Royer, Jr., *Biochemistry*, 2003, **42**, 4640-4647.
18. Y. Zhou, H. Zhou and M. Karplus, *J. Mol. Biol.*, 2003, **326**, 593-606.
19. J. E. Knapp, M. A. Bonham, Q. H. Gibson, J. C. Nichols and W. E. Royer, Jr., *Biochemistry*, 2005, **44**, 14419-14430.
20. Y. Seno, *J. Comput. Chem.*, 2006, **27**, 701-710.
21. Y. Kiyota, R. Hiraoka, N. Yoshida, Y. Maruyama, T. Imai and F. Hirata, *J. Am. Chem. Soc.*, 2009, **131**, 3852-3853.
22. J. E. Knapp, R. Pahl, J. Cohen, J. C. Nichols, K. Schulten, Q. H. Gibson, V. Srajer and W. E. Royer, Jr., *Structure*, 2009, **17**, 1494-1504.
23. N. Yoshida, T. Imai, S. Phongphanphanee, A. Kovalenko and F. Hirata, *J. Phys. Chem. B*, 2009, **113**, 873-886.
24. J. S. Hub, M. B. Kubitzki and B. L. de Groot, *PLoS Comput. Biol.*, 2010, **6**, e1000774.
25. S. Fischer, K. W. Olsen, K. Nam and M. Karplus, *Proc. Natl. Acad. Sci. U. S. A.*, 2011, **108**, 5608-5613.
26. P. Ceci, L. Giangiacomo, A. Boffi and E. Chiancone, *J. Biol. Chem.*, 2002, 277, 6929-6933K. Nienhaus, J. E. Knapp, P. Palladino, W. E. Royer, Jr. and G. U. Nienhaus, *Biochemistry*, 2007, 46, 14018-14031.
27. P. Ceci, L. Giangiacomo, A. Boffi and E. Chiancone, *J. Biol. Chem.*, 2002, 277, 6929-6933.

28. H. S. Cho, N. Dashdorj, F. Schotte, T. Graber, R. Henning and P. Anfinrud, *Proc. Natl. Acad. Sci. U. S. A.*, 2010, **107**, 7281-7286.
2829. E. Malmerberg, Z. Omran, J. S. Hub, X. Li, G. Katona, S. Westenhoff, L. C. Johansson, M. Andersson, M. Cammarata, M. Wulff, D. van der Spoel, J. Davidsson, A. Specht and R. Neutze, *Biophys. J.*, 2011, **101**, 1345-1353.
2930. D. Arnlund, L. C. Johansson, C. Wickstrand, A. Barty, G. J. Williams, E. Malmerberg, J. Davidsson, D. Milathianaki, D. P. DePonte, R. L. Shoeman, D. Wang, D. James, G. Katona, S. Westenhoff, T. A. White, A. Aquila, S. Bari, P. Berntsen, M. Bogan, T. B. van Driel, R. B. Doak, K. S. Kjaer, M. Frank, R. Fromme, I. Grotjohann, R. Henning, M. S. Hunter, R. A. Kirian, I. Kosheleva, C. Kupitz, M. Liang, A. V. Martin, M. M. Nielsen, M. Messerschmidt, M. M. Seibert, J. Sjohamn, F. Stellato, U. Weierstall, N. A. Zatsepin, J. C. Spence, P. Fromme, I. Schlichting, S. Boutet, G. Groenhof, H. N. Chapman and R. Neutze, *Nat. Methods*, 2014, **11**, 923-926.
3031. A. Bjorling, S. Niebling, M. Marcellini, D. van der Spoel and S. Westenhoff, *J. Chem. Theory Comput.*, 2015, **11**, 780-787.
3132. T. Konuma, T. Kimura, S. Matsumoto, Y. Goto, T. Fujisawa, A. R. Fersht and S. Takahashi, *J. Mol. Biol.*, 2011, **405**, 1284-1294.
3233. P. L. Ramachandran, J. E. Lovett, P. J. Carl, M. Cammarata, J. H. Lee, Y. O. Jung, H. Ihhee, C. R. Timmel and J. J. van Thor, *J. Am. Chem. Soc.*, 2011, **133**, 9395-9404.
3334. C. M. Summerford, A. Pardanani, A. H. Betts, A. R. Poteete, G. Colotti and W. E. Royer, Jr., *Protein Eng. Des. Sel.*, 1995, **8**, 593-599.
3435. H. Kim, J. G. Kim, S. Muniyappan, T. W. Kim, S. J. Lee and H. Ihhee, *J. Phys. Chem. B*, 2020, **124**, 1550-1556.
3536. J. G. Kim, S. Muniyappan, K. Y. Oang, T. W. Kim, C. Yang, K. H. Kim, J. Kim and H. Ihhee, *Struct. Dyn.*, 2016, **3**, 023610.
3637. K. H. Kim, S. Muniyappan, K. Y. Oang, J. G. Kim, S. Nozawa, T. Sato, S. Y. Koshihara, R. Henning, I. Kosheleva, H. Ki, Y. Kim, T. W. Kim, J. Kim, S. Adachi and H. Ihhee, *J. Am. Chem. Soc.*, 2012, **134**, 7001-7008.
3738. C. Yang, M. Choi, J. Kim, H. Kim, S. Muniyappan, S. Nozawa, S.-i. Adachi, R. Henning, I. Kosheleva and H. Ihhee, *Int. J. Mol. Sci.*, 2018, **19**, 3633.
3839. K. Y. Oang, C. Yang, S. Muniyappan, J. Kim and H. Ihhee, *Struct. Dyn.*, 2017, **4**, 044013.
3940. V. Srager, T. Teng, T. Ursby, C. Pradervand, Z. Ren, S. Adachi, W. Schildkamp, D. Bourgeois, M. Wulff and K. Moffat, *Science*, 1996, **274**, 1726-1729.

4041. E. Chen, M. J. Wood, A. L. Fink and D. S. Klier, *Biochemistry*, 1998, **37**, 5589-5598.
4142. V. Srager, Z. Ren, T. Y. Teng, M. Schmidt, T. Ursby, D. Bourgeois, C. Pradervand, W. Schildkamp, M. Wulff and K. Moffat, *Biochemistry*, 2001, **40**, 13802-13815.
4243. F. Schotte, M. Lim, T. A. Jackson, A. V. Smirnov, J. Soman, J. S. Olson, G. N. Phillips, Jr., M. Wulff and P. A. Anfinrud, *Science*, 2003, **300**, 1944-1947.
4344. M. Schmidt, K. Nienhaus, R. Pahl, A. Krasselt, S. Anderson, F. Parak, G. U. Nienhaus and V. Srager, *Proc. Natl. Acad. Sci. U. S. A.*, 2005, **102**, 11704-11709.
4445. R. t. Aranda, E. J. Levin, F. Schotte, P. A. Anfinrud and G. N. Phillips, Jr., *Acta Crystallogr., Sect. D: Biol. Crystallogr.*, 2006, **62**, 776-783.
4546. M. Cammarata, M. Levantino, F. Schotte, P. A. Anfinrud, F. Ewald, J. Choi, A. Cupane, M. Wulff and H. Ihee, *Nat. Methods*, 2008, **5**, 881-886.
4647. S. Ahn, K. H. Kim, Y. Kim, J. Kim and H. Ihee, *J. Phys. Chem. B*, 2009, **113**, 13131-13133.
4748. S. Westenhoff, E. Nazarenko, E. Malmerberg, J. Davidsson, G. Katona and R. Neutze, *Acta Crystallogr., Sect. A: Found. Crystallogr.*, 2010, **66**, 207-219.
4849. K. H. Kim, K. Y. Oang, J. Kim, J. H. Lee, Y. Kim and H. Ihee, *Chem. Commun.*, 2011, **47**, 289-291.
4950. K. Y. Oang, J. G. Kim, C. Yang, T. W. Kim, Y. Kim, K. H. Kim, J. Kim and H. Ihee, *J. Phys. Chem. Lett.*, 2014, **5**, 804-808.
5051. K. Y. Oang, K. H. Kim, J. Jo, Y. Kim, J. G. Kim, T. W. Kim, S. Jun, J. Kim and H. Ihee, *Chem. Phys.*, 2014, **422**, 137-142.
5152. J. G. Kim, T. W. Kim, J. Kim and H. Ihee, *Acc. Chem. Res.*, 2015, **48**, 2200-2208.
5253. A. Shimada, M. Kubo, S. Baba, K. Yamashita, K. Hirata, G. Ueno, T. Nomura, T. Kimura, K. Shinzawa-Itoh, J. Baba, K. Hatano, Y. Eto, A. Miyamoto, H. Murakami, T. Kumasaka, S. Owada, K. Tono, M. Yabashi, Y. Yamaguchi, S. Yanagisawa, M. Sakaguchi, T. Ogura, R. Komiya, J. Yan, E. Yamashita, M. Yamamoto, H. Ago, S. Yoshikawa and T. Tsukihara, *Sci. Adv.*, 2017, **3**, e1603042.
5354. T. W. Kim, S. J. Lee, J. Jo, J. G. Kim, H. Ki, C. W. Kim, K. H. Cho, J. Choi, J. H. Lee, M. Wulff, Y. M. Rhee and H. Ihee, *Proc. Natl. Acad. Sci. U. S. A.*, 2020, **117**, 14996-15005.
5455. C. Zang, J. A. Stevens, J. J. Link, L. Guo, L. Wang and D. Zhong, *J. Am. Chem. Soc.*, 2009, **131**, 2846-2852.

The structural and functional roles of the salt bridges in the allosteric structural transition of homodimeric hemoglobin are investigated by time-resolved x-ray solution scattering.



Supporting information

Effect of Abolition of Intersubunit Salt Bridges on Allosteric Protein Structural Dynamics

Minseo Choi,^{a,b,‡} Jong Goo Kim,^{b,‡} Srinivasan Muniyappan,^{b,‡} Hanui Kim,^{a,b} Tae Wu Kim,^b Yunbeom Lee,^{a,b} Sang Jin Lee,^{a,b} Seong Ok Kim,^b and Hyotcherl Ihee^{*,a,b}

^a*Department of Chemistry and KI for the BioCentury, Korea Advanced Institute of Science and Technology (KAIST), Daejeon 34141, Republic of Korea*

^b*Center for Nanomaterials and Chemical Reactions, Institute for Basic Science (IBS), Daejeon 34141, Republic of Korea*

*Corresponding author. Email: hyotcherl.ihee@kaist.ac.kr

‡These authors contributed equally to this work.

†Electronic Supplementary Information (ESI) available: See DOI: 10.1039/x0xx00000x

Data processing

Two-dimensional x-ray scattering patterns were azimuthally integrated to obtain one-dimensional scattering curves as a function of the magnitude of the momentum transfer vector, $q = (4\pi/\lambda)\sin(2\theta/2)$. To convert the scattering angle (2θ) to q , the center-of-mass position of the undulator spectrum was used as the reference wavelength (λ). Since a majority of scattering signal comes from solvent pairs or bulk solvent, the laser-induced scattering intensity changes are less than a few percent of the static scattering intensity. To extract the underlying scattering signal from solute molecules, we obtained time-resolved difference x-ray solution scattering curves at the time delay of t , $\Delta S(q, t)$, shown in Fig. S6 after careful normalization. As a normalization reference, we used a q position of 2.07 \AA^{-1} , which is the isosbestic point of the water scattering curves with respect to the temperature increase, so that the difference scattering intensity at this q value is zero. The scattering contribution arising from the solvent heating in the time-resolved difference x-ray solution scattering curves was removed by the following procedures. In Fig. S8, the solution scattering difference curve at 10 ms is presented as an example confirming that the difference scattering at late time delays ~~are~~is mainly attributed to solvent heating. The difference scattering curve is similar to the scattering curve arising from the water thermal heating, indicating that the contribution from transiently generated species is negligible. The signal where $q > 1.0 \text{ \AA}^{-1}$ can be represented by a thermal heating signal of bulk water, which is represented by a sum of the temperature change at a constant density $((\partial S(q)/\partial T)_\rho)$ and the density change at a constant temperature $((\partial S(q)/\partial \rho)_T)$. This fitted curve, represented by a linear combination of $((\partial S(q)/\partial T)_\rho)$ and $((\partial S(q)/\partial \rho)_T)$, was subtracted from the difference curves at all time delays to remove the solvent heating effect (see Fig. S7).

General scheme for the kinetic analysis using SVD and PCA

To extract kinetics information of intermediates and their structures from $\Delta S(q, t)$, we followed the well-established procedure, which had been applied to previous TRXSS studies on WT and various mutants of HbI, consisting of kinetic analysis using singular value decomposition (SVD) and principal component analysis (PCA). First, SVD, which is a factorization method to separate the time-dependent information from the time-independent information, was performed on the $\Delta S(q, t)$ matrix for the entire time points of 100 ps - 10 ms

and the q range of $0.17 - 1.0 \text{ \AA}^{-1}$, yielding left singular vectors (lSVs), right singular vectors (rSVs) and singular values. The lSVs, rSVs and singular values contain time-independent information, their time dependence, and their relative significance, respectively. Then, we conducted PCA, which is a method for generating theoretical difference scattering curves using time-dependent concentration changes of the intermediates expressed with a set of variable kinetic parameters, with an assumed candidate kinetic model from the results of SVD on the data matrix. Through PCA, we optimized kinetic parameters by fitting the experimental difference scattering curves with the theoretical difference scattering curves and obtained time-dependent concentration changes and species-associated difference scattering curves (SADSSs) of the corresponding intermediates.

SVD Analysis

To determine the kinetic model, we need to examine the number of distinct transient species in the dynamic process of interest and their associated rate coefficients. For this purpose, we applied the singular value decomposition (SVD) analysis and the subsequent kinetic analysis to our experimental data. From the experimental scattering curves measured at various time delays, we can build $n_q \times n_t$ matrix \mathbf{A} , where n_q is the number of q points in the scattering curve at a given time-delay point and n_t is the number of time-delay points. For the data in this work, n_q and n_t are 406 and 33, respectively. Then, the matrix \mathbf{A} can be decomposed while satisfying the relationship of $\mathbf{A} = \mathbf{U}\mathbf{S}\mathbf{V}^T$, where \mathbf{U} is an $n_q \times n_t$ matrix whose columns are called left singular vectors (lSVs) and contain time-independent q spectra, \mathbf{V} is an $n_t \times n_t$ matrix whose columns are called right singular vectors (rSVs) and contain time-dependent amplitude changes of the corresponding lSVs, and \mathbf{S} is a diagonal $n_t \times n_t$ matrix whose diagonal elements are called singular values. Since the diagonal elements (i.e. singular values) of \mathbf{S} , which represent the weight of lSVs in \mathbf{U} , are ordered so that $s_1 \geq s_2 \geq \dots \geq s_n \geq 0$, (both left and right) singular vectors on more left have larger contributions to the constructed experimental data. In this manner, we can extract the time-independent scattering intensity components from the lSVs, and the time evolution of their amplitudes from the rSVs, and their relative importance from the singular values. The lSVs, when combined, can give information on the scattering curves of distinct transient species, while the rSVs contain the information on the population dynamics of the transient species. Thus, the SVD analysis provides a model-independent estimation of the number of

structurally distinguishable species and the dynamics of each species. As shown in Figs. 2b and S9, the singular values and autocorrelation values of the corresponding singular vectors suggest that four singular vectors are enough to represent the experimental data of the K30D. The contribution from the ~~fourth~~^{fifth} singular vector and beyond becomes negligible. In this regard, the first four rSVs were simultaneously fit with the sum of five exponential functions, whose time coefficients were shared, resulting in common time constants of 4.616 (\pm 0.6657) ns, 46.647 (\pm 13.3) ns, 588 (\pm 80.681) ns, 616 (\pm 108109) μ s, and 5.34 (\pm 5.22) ms (see Fig. 2c). In summary, SVD and the global fit of rSVs show that the kinetics involves four intermediates and five time constants.

SVD with various reduced time ranges and SVD-aided pseudo PCA analysis (SAPPA) for determining the kinetic model

To establish the kinetic framework, we tried to obtain To establish the kinetic framework, we used two effective methods that can greatly facilitate narrowing down the kinetic models compatible with the experimental data: (i) the numbers of species from the SVD results on various reduced time ranges and (ii) SVD-aided pseudo PCA analysis (SAPPA).¹ First of all, we obtained clues about the number of intermediates associated with each of the relaxation times by performing the SVD analyses for various reduced time ranges in addition to the whole data.¹ For the SVD with a reduced time range, the upper limit close to and containing the value of each time constant obtained from the fitting of rSVs was chosen. Accordingly, four reduced time ranges (i) from 100 ps to 5.62 ns, (ii) from 100 ps to 56.2 ns, (iii) from 100 ps to 1 μ s, and (iv) from 100 ps to 1 ms were used for SVD analysis. The major ISVs from the SVD analysis for reduced and the entire ranges are shown in Fig. S10. The SVD result shows that the first time range from 100 ps to 5.62 ns has two main components, indicating that the first time constant of 4.616 ns can be explained as contributing to the transition from I₁-the first intermediate (A) to I₂-the second intermediate (B). The SVD results on the second time range from 100 ps to 56.2 ns and the third range from 100 ps to 1 μ s reveal that the number of main components increases to and remains at three, which means that the two time constants of 46.6 ns and 588 ns need to be assigned to the biphasic transition from I₂ to I₃. As a result, among five time constants, two (616 μ s and 5.34 ms) remain to be assigned. Adding the third intermediate (C) satisfying this condition allows for the nine kinetic frameworks shown in Fig. S14.

To further narrow down the kinetic frameworks compatible with the experimental data, we used the SAPPA method. In SAPPA, time zones that show stationary temporal behavior in the major rSVs are identified, and the experimental data at those identified stationary time zones are used as the basis to fit the experimental data at each time delay. The number of necessary time zones is the same as the number of the main components in the time range of interest, that is, three in the time range from 100 ps to 10 μ s. Inspection of the first three rSVs multiplied by corresponding singular values (Fig. 2c) shows that the time zones around 100 ps, 10 ns, and 10 μ s satisfy the stationary condition (that is, the rSVs do not change much with time). Then we used the experimental difference curves corresponding to these three time zones (more specifically, the difference curves at 100 ps, 10 ns, and 10 μ s) to fit the corresponding contribution at each time delay. The obtained profiles are shown in Fig. S15a. These profiles already show the general kinetic framework containing A \rightarrow B \rightarrow C. At this point, it is worth noting that three, the number of main components for the second time range from 100 ps to 56.2 ns, is compatible with the parallel kinetic framework containing both A \rightarrow B and A \rightarrow C as well as the sequential one containing A \rightarrow B \rightarrow C. The SAPPA kinetic profiles rule out the parallel framework. For this reason, we showed only those with the sequential one in Fig. S14 (to avoid unnecessary complexity that may confuse readers).

While this simple framework of A \rightarrow B \rightarrow C needs only two time constants, three time constants obtained from rSVs (4.6 ns, 47 ns, 588 ns) indicate that there should be one more kinetic process involved. Fitting these profiles using these time constants show the most natural scenario is that 4.6 ns accounts for A \rightarrow B and both 47 ns and 588 ns account for B \rightarrow C, meaning that a B-to-C biphasic transition (model (6) in Fig. S14). Moreover, a comparison of the SAPPA kinetic profiles (Fig. S15b) and the expected kinetic profiles of the nine candidate frameworks (Fig. S15c) immediately allows for ruling out models (1) ~ (5), (8), and (9), whereas those of models (6) and (7) are compatible with the SAPPA profiles. Among these two models, only model (6) contains the biphasic transition from the second intermediate to the third intermediate, which is one of the common features observed in WT and all other mutants (F97Y, T72V, and I114F) studied by TRXSS. In other words, if A, B, and C are assigned to I₁, I₂, and I₃, respectively, model (6) is the same as the kinetic framework of WT, F97Y, T72V, and I114F. It should be noted that the I₂-to-I₃ biphasic transition originates from the existence of both fully photolyzed and partially photolyzed forms. The fully photolyzed form converts faster than the partially photolyzed form due to the allosteric effect. One cannot rule out the possibility of model (7), but we consider this

model highly unlikely because it is difficult to find any reason justifying why only the dimer of K30D shows such a drastically different kinetic framework.

The identity of one intermediate among four remains to be determined. This remaining intermediate can be either a monomer or a dimer. Nevertheless, we favor the possibility of a “monomer” intermediate for the following reasons. First, the K30D mutant has a weakened network of interaction between Asp30 and Asp89 located in the subunit interface. In WT, there are intersubunit contacts involving the E and F helices, and the Lys30 residue, which has the form of cationic ammonium with a positive charge, is located near the linker connecting the E and F helices. As shown in the enlarged view of the interface with the two residues in Fig. 1, Lys30 in one subunit and Asp89 in the other subunit interact with each other by forming salt bridges and serve as bridges connecting the upper and lower subunits. The K30D mutation induces repulsive force between the negative charge of Asp30 introduced by the mutation and the negative charge of Asp89 in the other subunit, and consequently, the attraction between the two subunits is significantly weakened. The weakened interaction can increase the monomer proportion, and thus it is plausible that the additional intermediate, which was not observed for WT and mutants studied so far, is related to the monomer of the K30D. A study reported that the CO ligated form of WT has the dimerization constant of $2.2 \times 10^8 \text{ M}^{-1}$ at 25°C ,² which corresponds to the monomer ratio of 0.0003% in aqueous solution. By contrast, K30D has a dimerization constant of $1.2 \times 10^3 \text{ M}^{-1}$ at 10°C ³ under the equivalent condition and the ratio of the monomer is 41% in aqueous solution. Considering that our TRXSS experiment was conducted at room temperature (25°C), the monomer ratio should be even higher than that reported for 10°C . Second, the K30D monomer can be regarded as a monomeric heme protein such as myoglobin and cytochrome c, whose photoinduced structural changes were observed in many time-resolved studies,⁴⁻¹⁹ and thus it is plausible that the K30D monomer undergoes the structural change induced by photoexcitation. Third, the simulated difference scattering intensity of the monomer showed a magnitude that cannot be neglected compared to that of the dimer. To check if TRXSS data can be sensitive to the structural change of the monomer, we simulated the difference scattering curves by simply splitting the carboxy form and intermediates of WT HbI in half and assuming that the same structural changes occurring in the WT dimer occur in the WT monomer (Fig. S3). Surprisingly, even if the monomer is half the dimer's size, the difference scattering intensity of the monomer is similar to that of the dimer in the q range of $0.17 - 1.0 \text{ \AA}^{-1}$, or even larger in certain q regions. Therefore, the kinetic analysis was

performed assuming a framework that included the photoinduced structural change of the dimeric form of K30D HbI(CO)₂ and the monomeric form of K30D HbI(CO)₂.

Assignment of time constants for bimolecular CO recombination

To discuss the kinetic model containing the monomer, we consider the issue of assigning time constants of 616 μ s and 5.34 ms. In previous studies for most of the heme proteins such as the WT HbI, its mutants, Hb, and Mb, the bimolecular rate of the recovery from the last intermediate (I_3 in the case of HbI) to the initial CO-ligated state was approximated as a biexponential function using two rate constants observed in rSVs.²⁰⁻²² For the same approach to be applied to the case of K30D, where two intermediates, I_3 and i , instead of a single intermediate, undergo bimolecular CO recombination, four time constants (two per each intermediate) are required whereas only two time constants (616 μ s and 5.34 ms) were identified from SVD. To identify the root of this situation, we checked the difference signal of the whole time delay and noticed that the difference curve at 10 ms still has a remaining difference signal, which means that the CO recombination is not fully completed within the time range of our experiment. If the data had been collected at time delays later than 10 ms, time constants larger than 5.34 ms would have been extracted, giving exponential time constants more than two. Considering this fact and given the possible combinations of the two time constants, the situations that best describe the data are the following two cases. In the first case, model (a) (Fig. S11a), the time constants of 616 μ s and 5.34 ms are assigned to the bimolecular CO recombination of i that is already generated in the time resolution (< 100 ps) and 5.34 ms being the time constant reused for I_3 returning to HbI(CO)₂. In the second case, model (b) (Fig. S11b), on the contrary, two time constants are assigned to CO recombination of I_3 and 5.34 ms is reused to CO recombination of i . Both kinetic models shown in Figs. S11a and S11b are compatible with the SVD results in the reduced and whole time ranges and fully explain the TRXSS data. The two models have the same kinetic framework, but in the case of the model (a), the CO recombination rate of I_3 is slower compared to that of i , and in the case of the model (b), the opposite. Among these two possible kinetic models, we finally propose the kinetic model (a) for the following reasons. Models (a) and (b) give different fractions of monomers in addition to the different recombination rates from I_3 to HbI(CO)₂. A TRXSS study of Mb shows that its CO recombination rate (230 mM⁻¹s⁻¹)¹⁵ is faster than that of WT HbI (95 mM⁻¹s⁻¹). This consideration renders that the monomer of K30D is likely to have faster CO recombination

than the dimer. Besides, it is natural that the fraction of the monomer is higher than that of the dimer under our experimental condition, and thus we can exclude model (b) where the monomer is almost absent (~0.3%, shown in Fig. S11b).

Kinetic analysis

From the SVD analysis and global fit of rSV, the first four singular vectors of significant singular values and five time constants were obtained. We performed the kinetic analysis using these four singular vectors and time constants. New matrices for K30D, \mathbf{U}' , \mathbf{V}' , and \mathbf{S}' , can be defined by removing non-significant components from \mathbf{U} , \mathbf{V} , and \mathbf{S} , respectively. In other words, \mathbf{U}' is an $n_q \times 4$ matrix containing only the first four left singular vectors of \mathbf{U} , \mathbf{S}' is a 4×4 diagonal matrix containing the first four singular values of \mathbf{S} , and \mathbf{V}' is an $n_q \times 4$ matrix containing the first four right singular vectors of \mathbf{V} . Here we represent the time-dependent concentrations of transiently formed intermediate species, which can be calculated from a kinetic model, by a matrix \mathbf{C} . Then, the matrix \mathbf{C} can be related to \mathbf{V}' by using a parameter matrix \mathbf{P} that satisfies $\mathbf{V}' = \mathbf{CP}$. In our analysis, \mathbf{C} is an $n_q \times 4$ matrix containing the time-dependent concentrations of four intermediates of K30D HbI, that is, the dimer intermediates of I_1 , I_2 , I_3 , and the monomer intermediate of i , and \mathbf{P} is a 44 matrix containing coefficients for the time-dependent concentrations so that the linear combination of concentrations of the three intermediates can form the three right singular vectors in \mathbf{V}' . Once \mathbf{C} is specified by a kinetic model with a certain set of variable kinetic parameters such as rate coefficients, \mathbf{P} and \mathbf{C} can be optimized by minimizing the discrepancy between \mathbf{V}' and \mathbf{CP} . However, standard deviations for \mathbf{V}' are not available from the experimental data, and thus we instead used the following method to optimize \mathbf{P} and \mathbf{C} . Since $\mathbf{V}' = \mathbf{CP}$, the following equation holds.

$$\mathbf{A}' = \mathbf{U}'\mathbf{S}'\mathbf{V}' = \mathbf{U}'\mathbf{S}'(\mathbf{CP})^T = \mathbf{U}'\mathbf{S}'(\mathbf{P}^T\mathbf{C}^T) = (\mathbf{U}'\mathbf{S}'\mathbf{P}^T)\mathbf{C}^T \quad (1)$$

where \mathbf{A}' is an $n_q \times n_t$ matrix that contains the theoretical difference scattering curve $\Delta S_{theory}(q_i, t_j)$ at given q and t values. Theoretical difference scattering curves calculated by using Eqn. (1) were compared with the experimental difference scattering curves, and the matrices \mathbf{P} and \mathbf{C} were optimized by minimizing the discrepancy χ^2 between the theoretical and experimental difference scattering curves. From Eqn. (1), we can define a matrix \mathbf{B} as $\mathbf{B} = \mathbf{U}'\mathbf{S}'\mathbf{P}^T$, that is, a linear combination of the three left singular vectors in \mathbf{U}' weighted by their singular values in \mathbf{S}' with their ratios determined by \mathbf{P} . Then, the matrix \mathbf{B} , an $n_q \times 4$ matrix,

contains the four difference scattering curves directly associated with the four intermediate species of K30D HbI. As a result of the kinetics analysis, we could determine the optimum kinetic parameters (Table S1) and extract the time-independent SADSSs (Fig. 3b) and time-dependent concentration changes (Fig. 3c) of the four intermediates.

Generation of the template structures for the structural analysis

Up to date, TRXSS studies on HbI have been performed with structure refinement applied with a rigid-body modeling approach using crystallographic structures as template structures.²²⁻²⁵ In the case of K30D, however, this method could not be applied because crystallographic structures were not reported, unlike WT or other mutants. HbI is a homodimeric protein with two symmetric subunits consisting of 16 α -helices, 14 linkers, and two heme groups. The proportion of α -helices accounts for about 80% of the total number of residues, and the protein is considered to be a relatively rigid protein because the α -helices are closely packed together. Also, the visible absorption spectra and circular dichroism spectra of WT and K30D HbI are nearly identical to each other for both liganded and unliganded forms, indicating high similarity in the local structure near the heme pocket in WT and K30D HbI.³ We, therefore, assumed that the backbone of WT and K30D would be quite similar to each other and generated hypothetical crystallographic structures of K30D by incorporating single amino acid residue replacements from the crystallographic structure formed at 5 ns after the photolysis of carbonyl ligand (PDB ID: 2GRZ) and the crystallographic structure of the carboxy form of WT HbI (PDB ID: 3SDH). The resulting structures were used as template structures in the structure refinement for K30D. The original crystallographic structures were modified using PyMol software by replacing Lys30 residues of two subunits of the HbI with Asp30 residues.

Structure refinement

The structure refinement using SADSSs of all intermediates of the K30D was performed. The positions and orientations of the rigid bodies were randomly generated based on a Monte Carlo simulation algorithm and refined to minimize the discrepancy between the theoretical difference scattering curve calculated from the refined structure and the SADSSs of the dimer and monomer intermediates. For each intermediate, the refinement process was repeated for 360 different initial structures whose rigid bodies were randomly displaced from the template. We selected 195, 167, 200, and 196 candidate structures for the I_1 , I_2 , I_3 and i ,

respectively, which exhibited χ^2 values (a quantified value of the discrepancy between the experimental and theoretical difference scattering curves) below a certain threshold. The theoretical difference scattering curves for the refined candidate structures are shown in Fig. S4.

Supporting information table and figures**Table S1.** Kinetic parameters obtained from the kinetic analysis of TRXSS data of K30D.

Parameters	Fit values
Time constant for I ₁ -to-I ₂ transition	4.6 (\pm 0.7) ns
Fast time constant for I ₂ -to-I ₃ transition	47 (\pm 13) ns
Slower time constant for I ₂ -to-I ₃ transition	558 (\pm 81) ns
Rate constant for bimolecular CO recombination of dimer (I ₃)	36.1 (\pm 3.31) mM ⁻¹ s ⁻¹
Rate constant for bimolecular CO recombination of monomer (<i>i</i>)	309 (\pm 8.57) mM ⁻¹ s ⁻¹
Fraction of dimer	19 (\pm 0.41) %
Fraction of fully photolyzed forms	38 (\pm 0.006) %

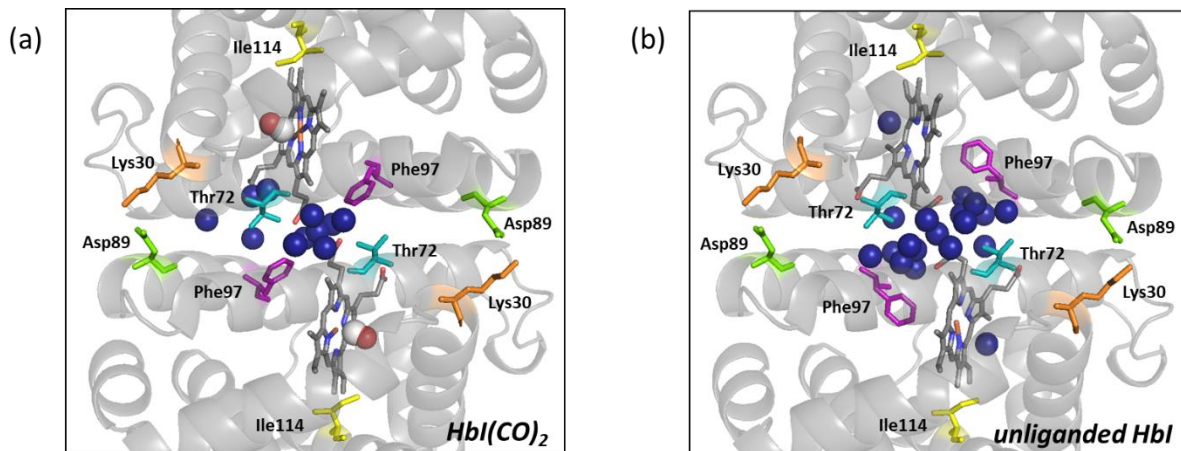


Fig. S1- (a) Enlarged view of the crystal structure of WT HbI(CO)₂ (PDB ID: 3SDH) and (b) unliganded WT HbI (PDB ID: 4SDH). Eleven and seventeen interfacial water molecules for HbI(CO)₂ and unliganded HbI, respectively, are shown with blue spheres. Heme-bounded CO molecules are shown with connected red and white spheres. The residues regulating the cooperative ligand binding and allosteric structural transition of HbI are indicated by sticks. Phe97, Thr72, Ile114, Lys30, and Asp89 are represented in purple, teal, yellow, orange, and light green colors, respectively.

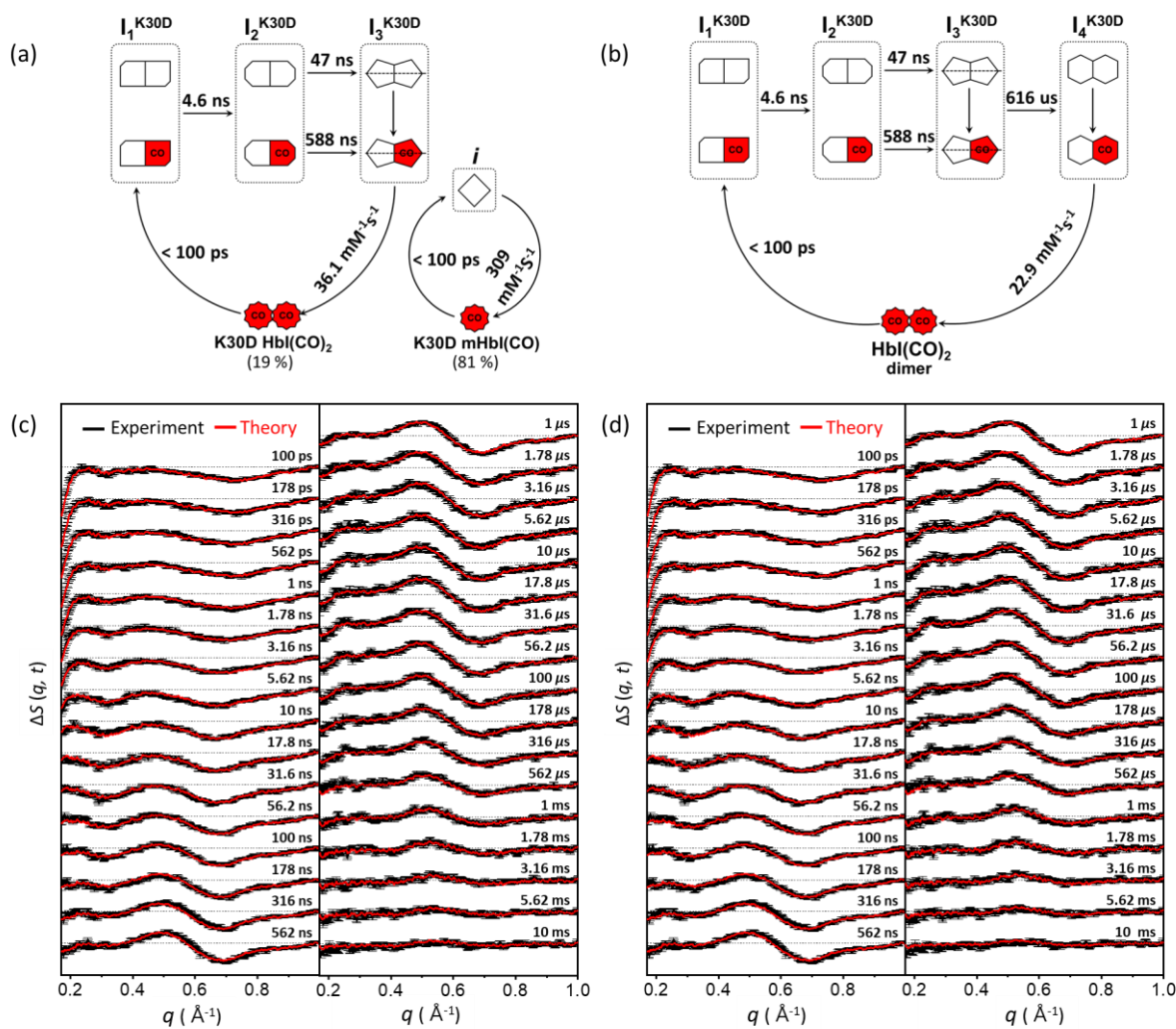


Fig. S2- (a, b) Kinetic models for the two scenarios where the fourth species are assumed to be (a) the monomer intermediate, *i*, and (b) the dimer intermediate, I_4^{K30D} . (c, d) Time-resolved x-ray solution scattering curves, $\Delta S(q, t)$, measured for a solution sample of K30D (black curves) are compared with theoretical curves (red curves) generated by linear combinations of left singular vectors (LSVs) based on the kinetic models where the fourth species is assumed to be (c) the monomer intermediate, *i*, and (d) the dimer intermediate, I_4^{K30D} . The calculated curves from both scenarios give equally satisfactory agreement with the experimental data.

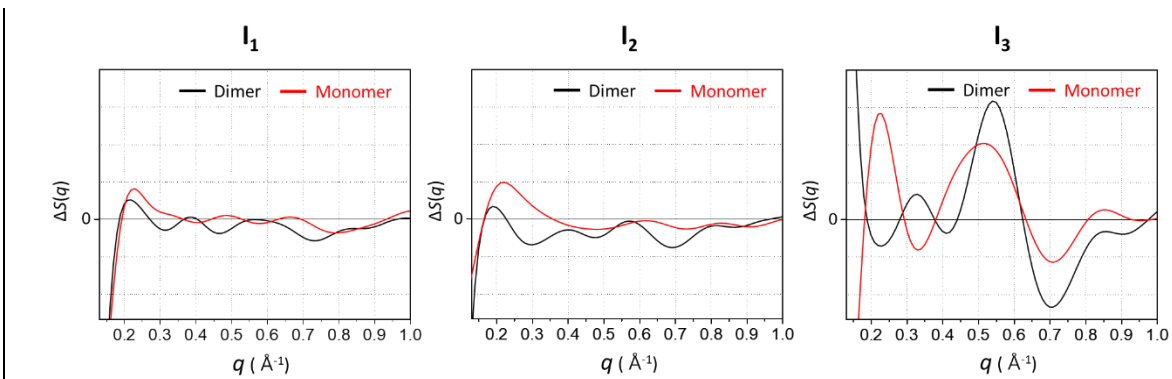


Fig. S3- Simulated difference scattering curves for the structural transition of the monomer and dimer of WT HbI for all three intermediates (I_1 , I_2 , and I_3). To simulate the structural transition of the monomer, both the crystallographic structure of the liganded form (PDB ID: 3SDH) and the intermediates of WT HbI were simply split into two halves and the corresponding scattering curve was calculated for the generated monomers of the liganded form and intermediates with the assumption that the same structural changes occurring in the WT dimer occur in the WT monomer. Difference scattering curves of the dimer are shown in black and the monomer difference scattering curves of the monomer are shown in red.

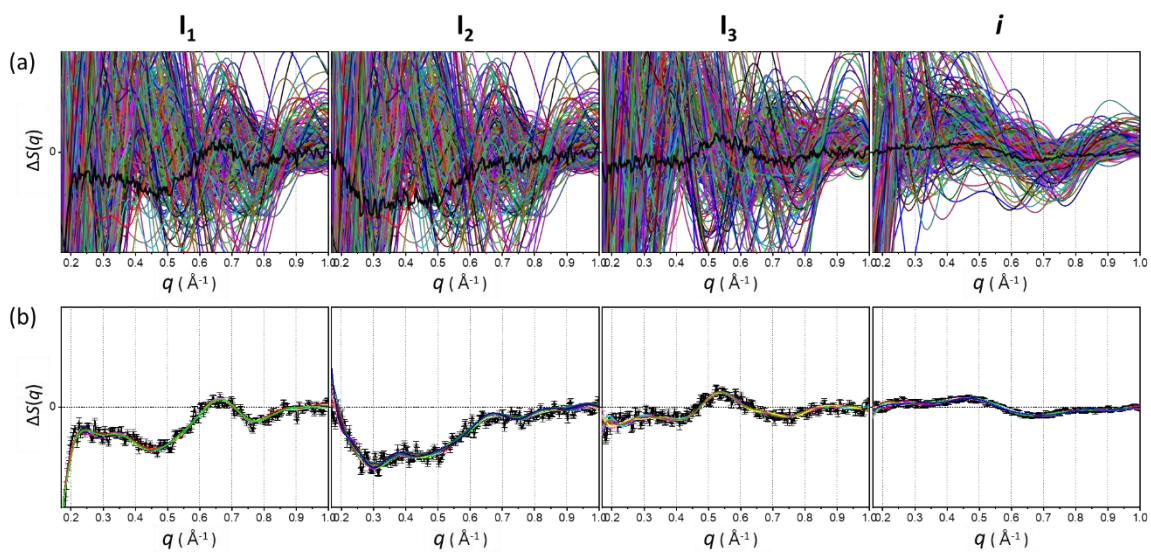


Fig. S4. (a) Comparison of the experimental SADSSs of all intermediates I_1 , I_2 , I_3 , i (black curves) with the theoretical scattering curves of the 360 randomly generated initial structures (color lines). (b) Comparison of the experimental SADSSs of all intermediates I_1 , I_2 , I_3 , i (black lines) with the experimental standard deviation and the theoretical scattering curves (color lines) from the best fit structures.

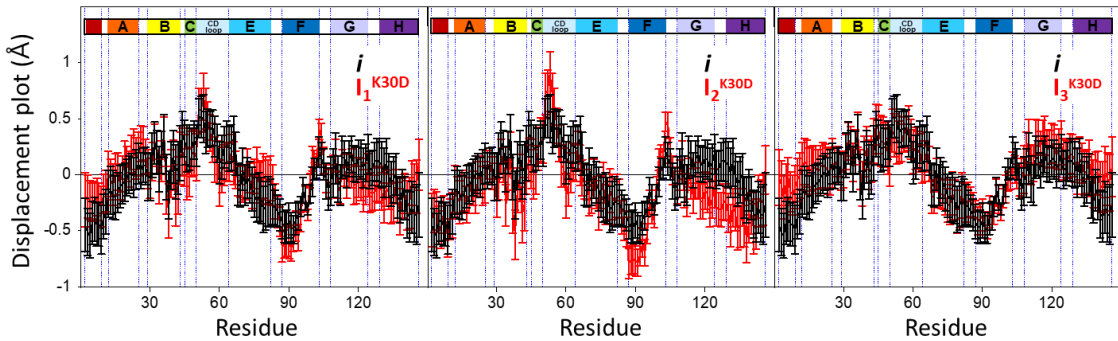


Fig. S5- The averaged displacement plots of the candidate structures for the monomer intermediate *i* (black), and the dimer intermediates (red) for I_1^{K30D} (left), I_2^{K30D} (middle), and I_3^{K30D} (right) were calculated with respect to the half of the mutated liganded crystal structure of WT (mutated from 3SDH). Error bars represent standard deviation values among various candidate structures of each intermediate.

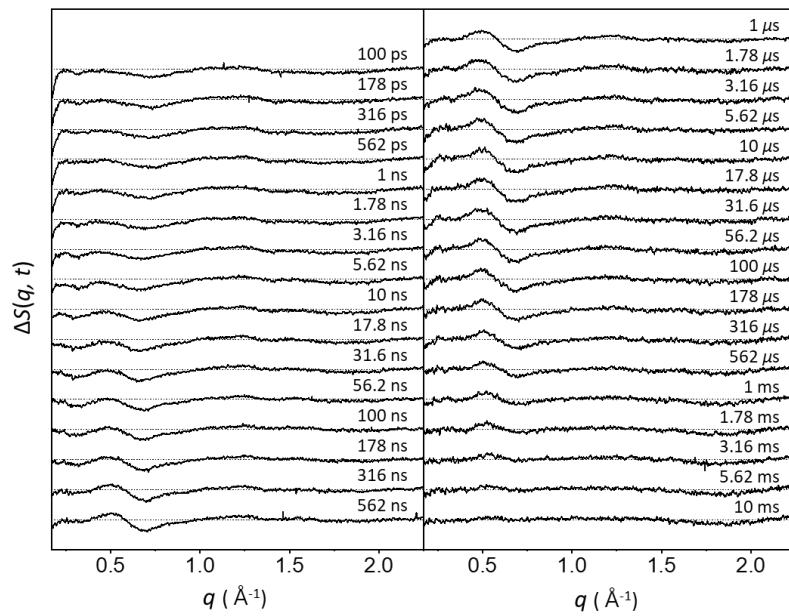


Fig. S6. Time-resolved difference x-ray solution scattering curves of K30D. We used q position of 2.07 \AA^{-1} as a normalization reference so that the difference scattering intensity at this q point is zero.

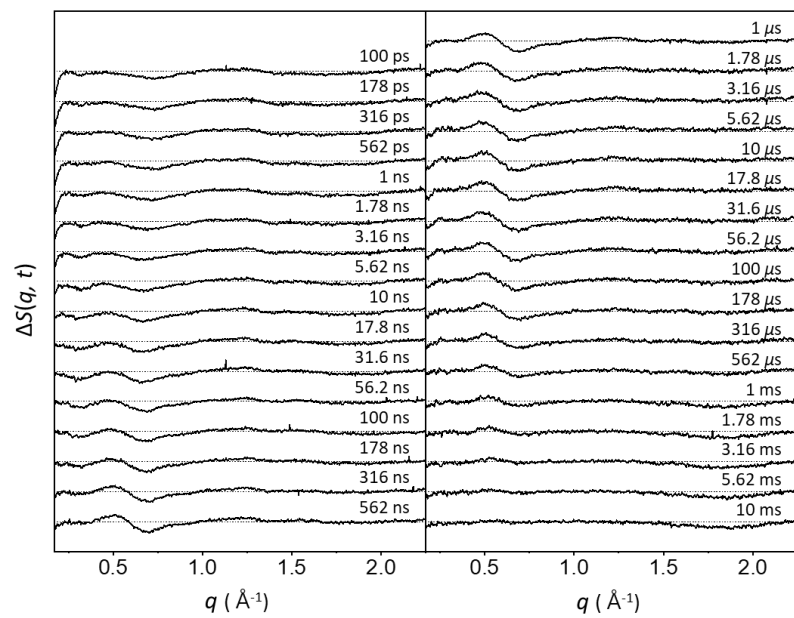


Fig. S7- Heat-free, time-resolved difference x-ray solution scattering data of K30D. The thermal heating signal of bulk water shown in Fig. S8 was subtracted from the original difference curves shown in Fig. S6.

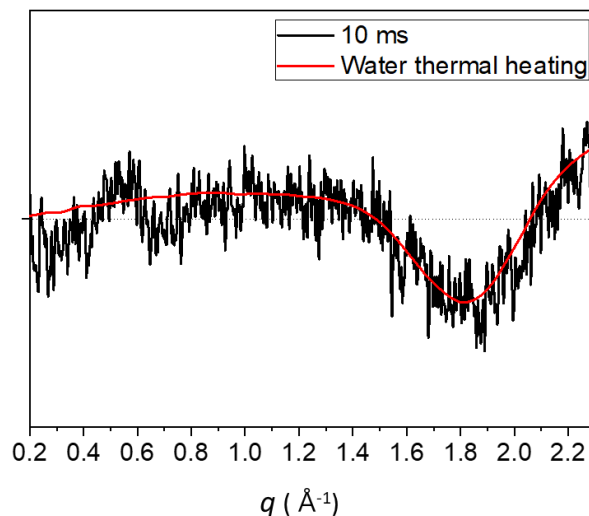


Fig. S8- The difference solution scattering curve at 10 ms (black) time delay. At this time delay, the difference scattering curve is similar to the scattering intensity change upon a temperature increase of the water solvent (red), indicating that the contribution from transiently generated species is negligible. More specifically, the signal in the region where $q > 1.0 \text{\AA}^{-1}$ can be represented by a heating signal of bulk water, which can be represented by a sum of the temperature change at constant density ($(\partial S(q)/\partial T)_\rho$) and the density change at constant temperature ($(\partial S(q)/\partial \rho)_T$). In other words, the difference signals at late time delays are mainly attributed to solvent heating.

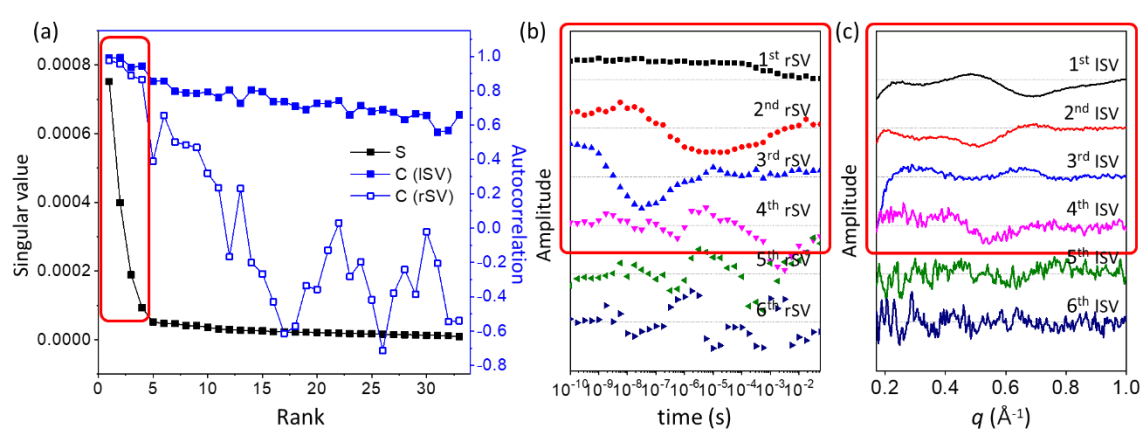
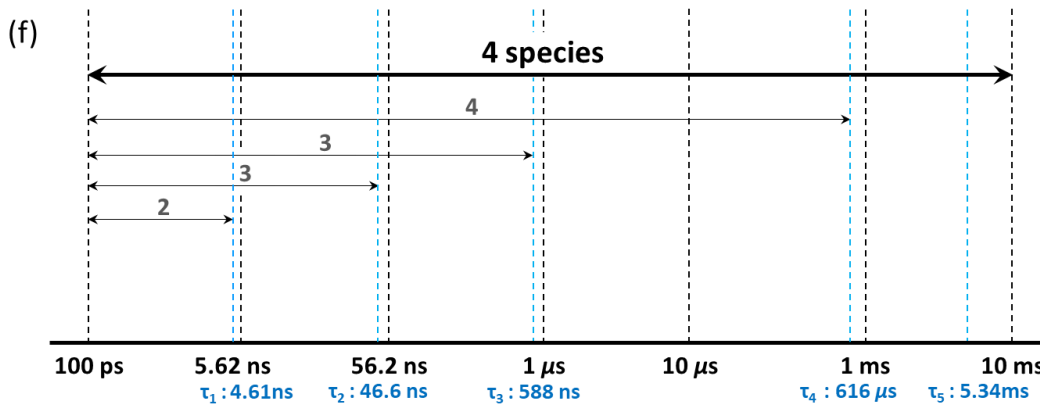
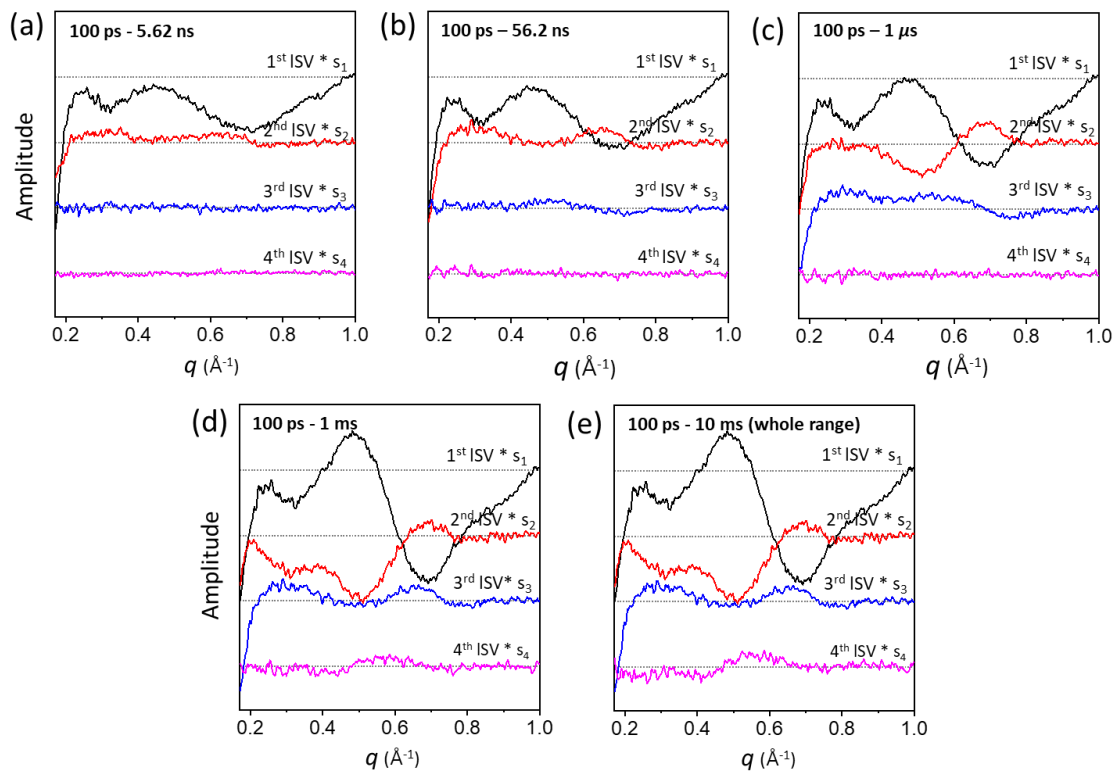


Fig. S9. (a) Singular values (solid black square), autocorrelations of left singular vectors, ISV, (solid blue square) and right singular vectors, rSVs, (blue open square) were obtained from TRXSS data. The first four (both left and right) singular vectors were selected for our kinetic analysis. (b) The first six rSVs are shown. (c) The first six rSVs are shown.



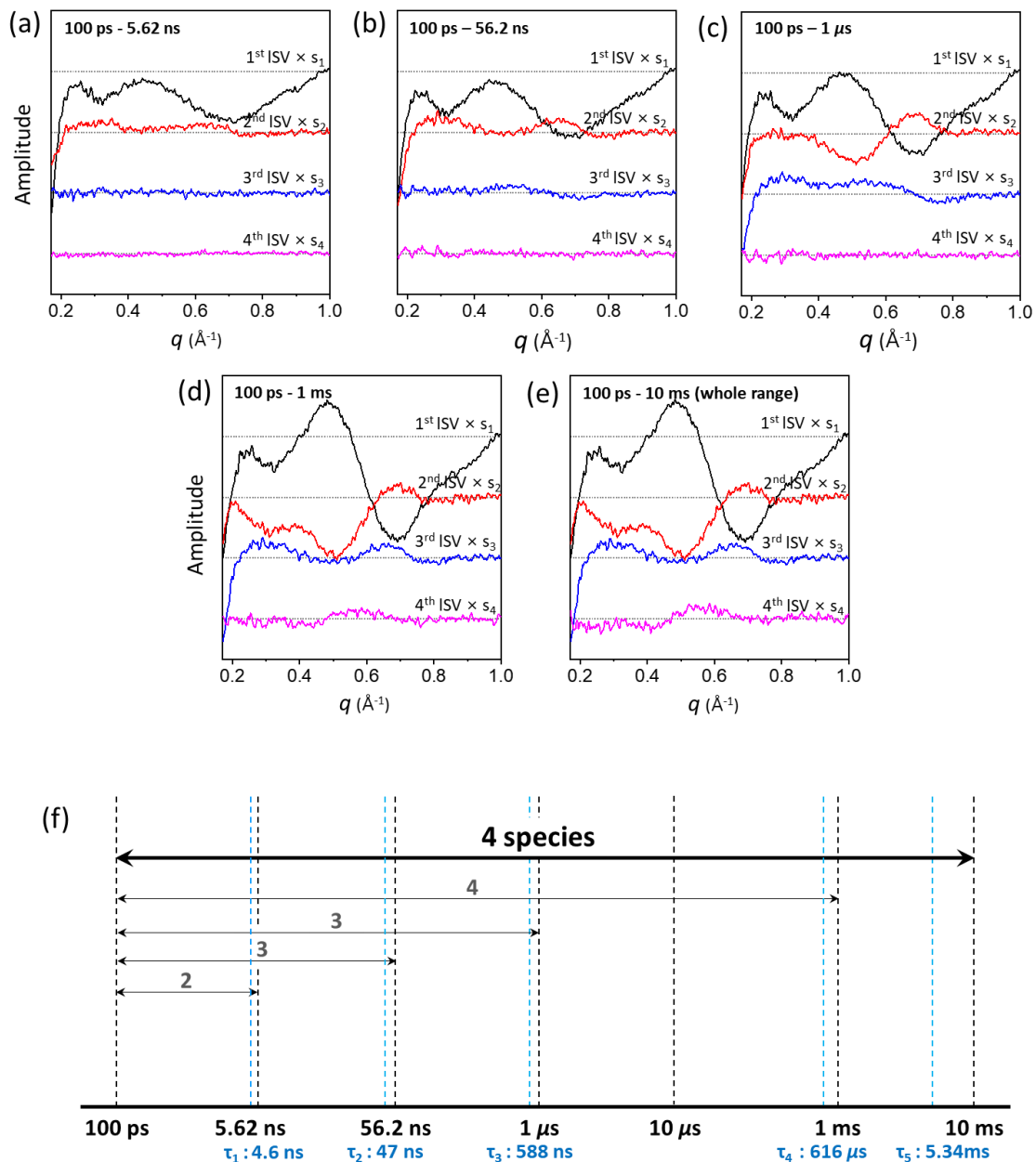


Fig. S10. The result of SVD analysis in six different time ranges. The first four ISVs multiplied by singular values in the reduced time ranges of (a) 100 ps - 5.62 ns, (b) 100 ps - 56.2 ns, (c) 100 ps - 1 μ s, (d) 100 ps - 1 ms, and (e) entire time range. As shown in Fig. (a), for example, two singular components of significant amplitudes were identified in this reduced time range of 100 ps - 5.62 ns. Various reduced time ranges, whose upper limit is close to and containing the value of each time constant, are shown in (f).

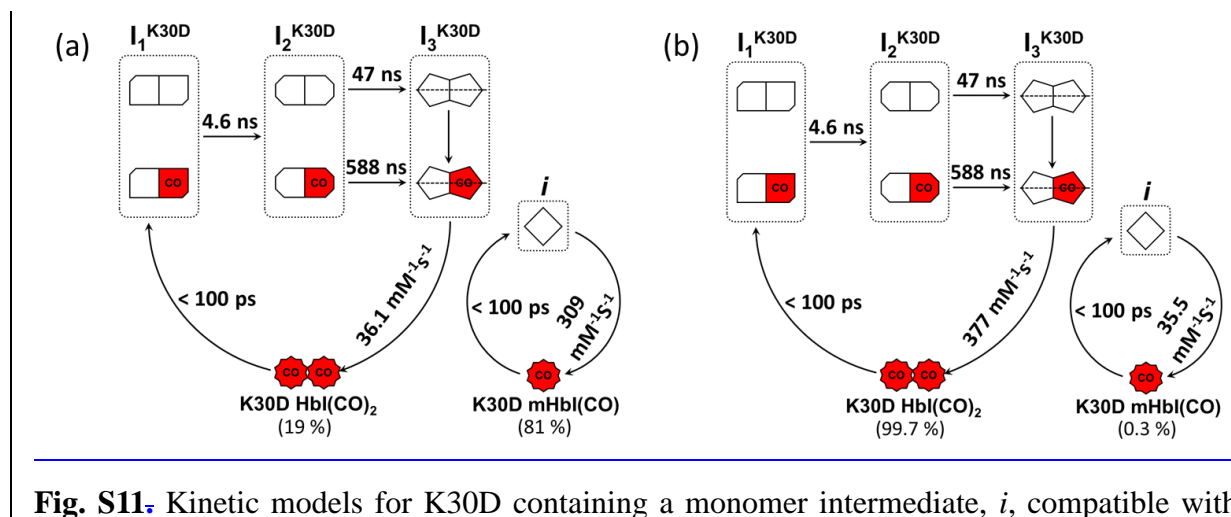


Fig. S11. Kinetic models for K30D containing a monomer intermediate, i , compatible with the SVD results in various time ranges. The red (with “CO”) and white symbols represent liganded and photolyzed subunits, respectively. To indicate the four structurally distinguishable intermediates with different tertiary structures, the subunit of each intermediate is presented with a different shape. In the kinetic model shown in (a), the bimolecular CO recombination of the monomer is faster than that of the dimer. In contrast, in the kinetic model shown in (b), the bimolecular CO recombination of the monomer is slower than that of the dimer.

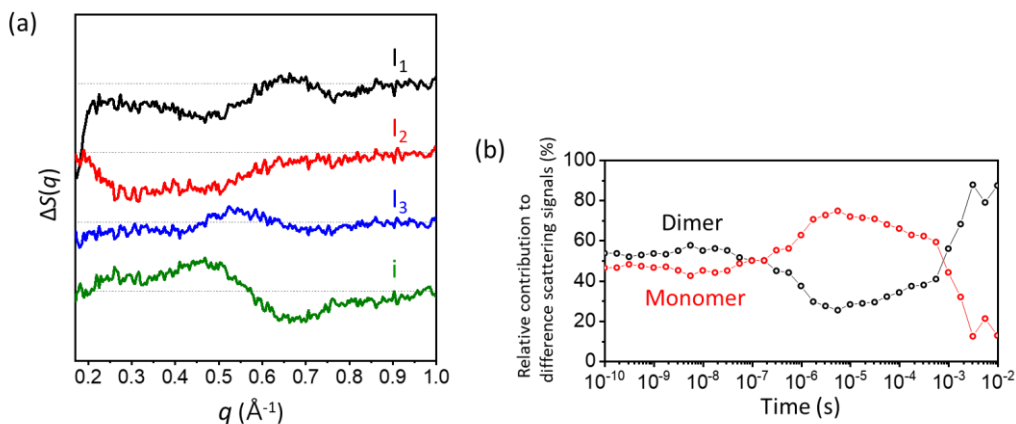


Fig. S12 (a) SADSs multiplied by the maximum concentrations of the four species (0.70 mM for I_1 , 0.64 mM for I_2 , 0.72 mM for I_3 , and 2.91 mM for i). This figure confirms that the contribution of dimers is comparable to that of monomers. More importantly, the magnitudes of SADSs are substantially larger than the noise level, indicating that the signal-to-noise ratio of the current data is enough to provide information for both dimers and monomers. (b) The relative contributions of dimers and monomers to the difference scattering signals as a function of time.

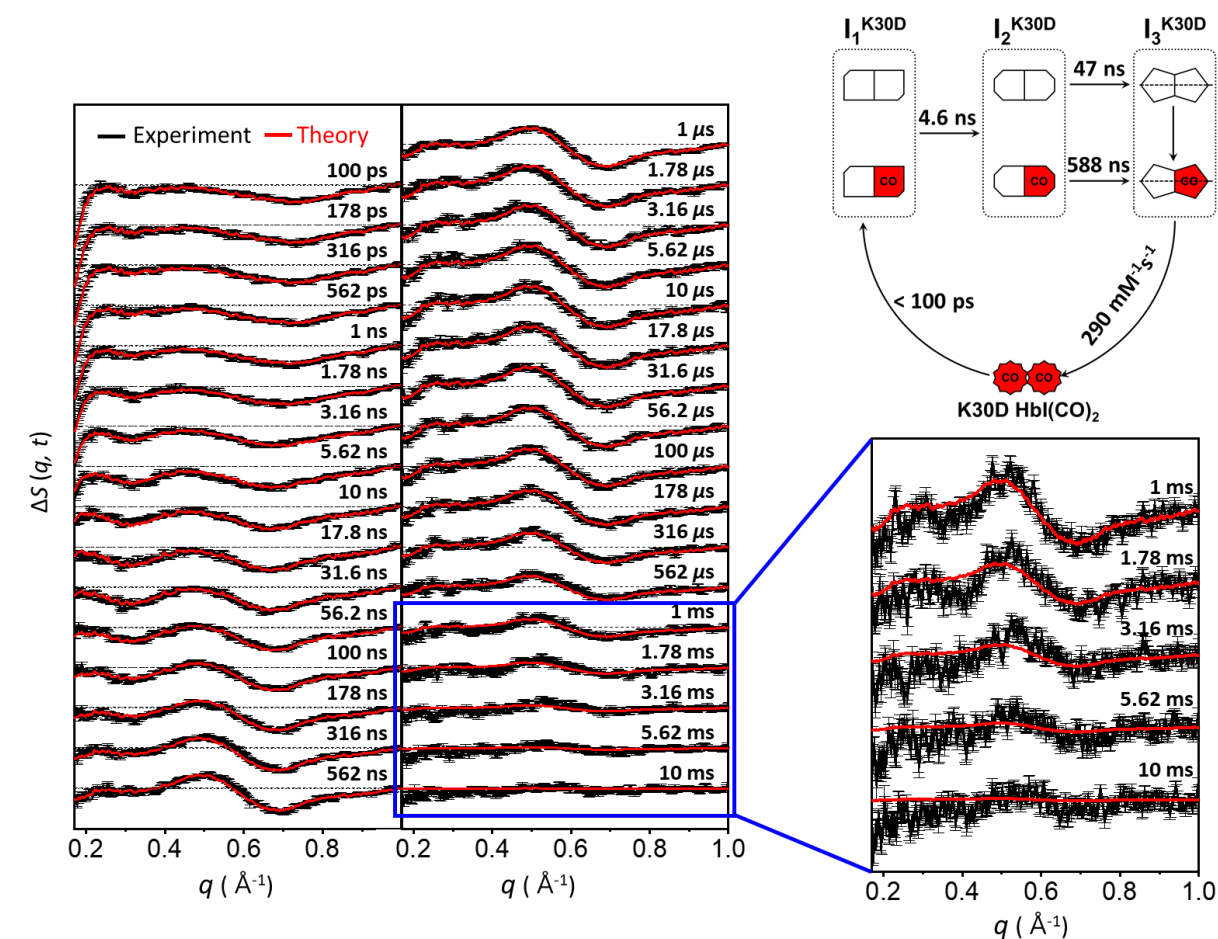


Fig. S13 Time-resolved x-ray solution scattering curves, $\Delta S(q, t)$, measured for a solution sample of K30D (black curves) are compared with theoretical curves (red curves) generated by linear combinations of only three ISVs instead of four, based on the kinetic model with only three dimer intermediates (I_1 , I_2 , and I_3) without the monomer intermediate (i). Note that the fit quality is significantly worse than those including the fourth intermediate in Fig. S2. The chi-square value increases by 21%.

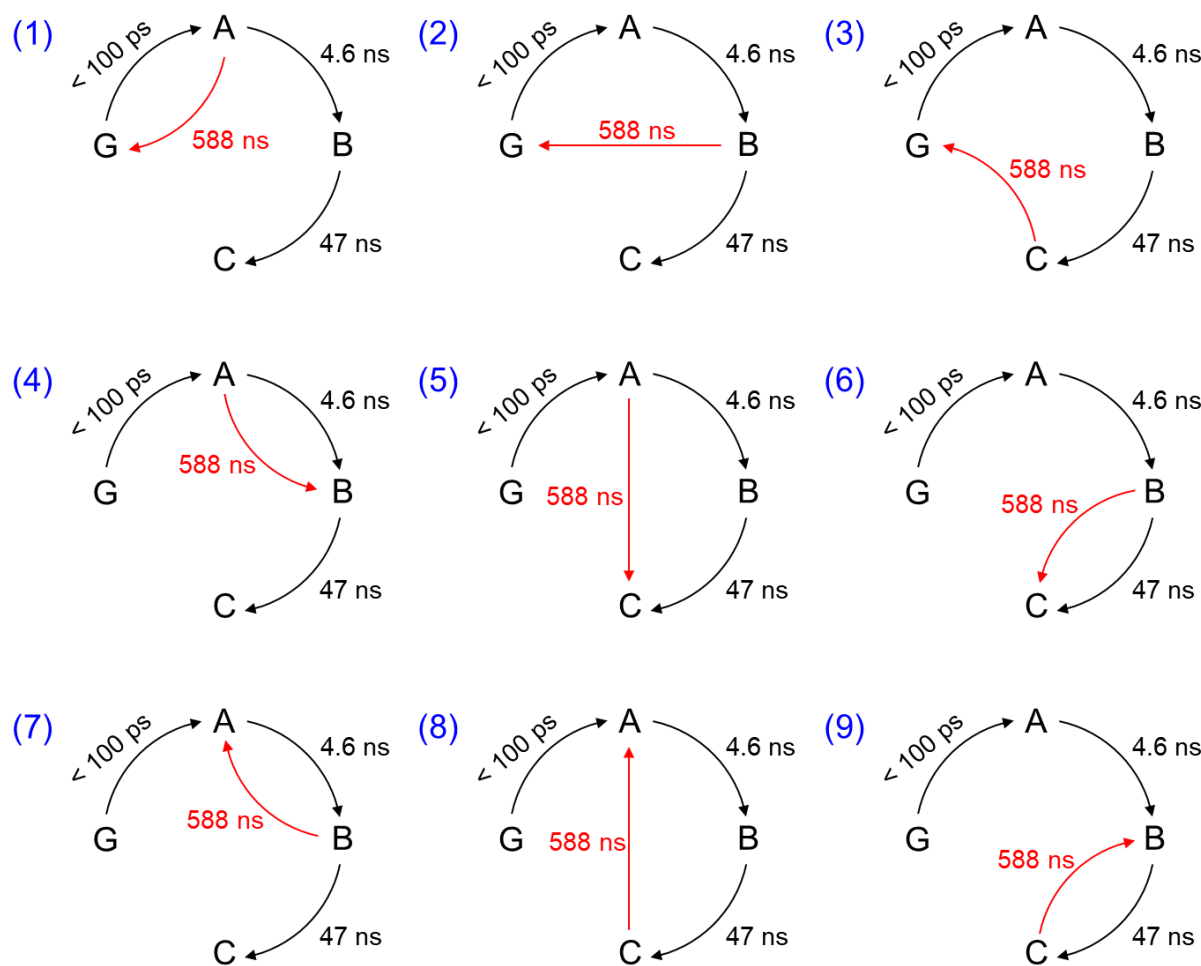


Fig. S14 All possible candidate kinetic models for the time range from 100 ps to 10 μ s, containing the sequential kinetic framework of $G \rightarrow A \rightarrow B \rightarrow C$ indicated by black arrows, where G, A, B, and C refer to the ground state, the first intermediate, the second intermediate, and the third intermediate, respectively. In all kinetic models, time constants of 4.6 ns and 47 ns are commonly assigned to $A \rightarrow B$ and $B \rightarrow C$ transitions, respectively, to be compatible with the results of SVD analyses in the reduced time ranges shown in Fig. S10. The kinetic models (1) ~ (9) are distinguished from each other in terms of the assignment of the time constant of 588 ns. In each kinetic model, the assignment of 588 ns is indicated by a red arrow.

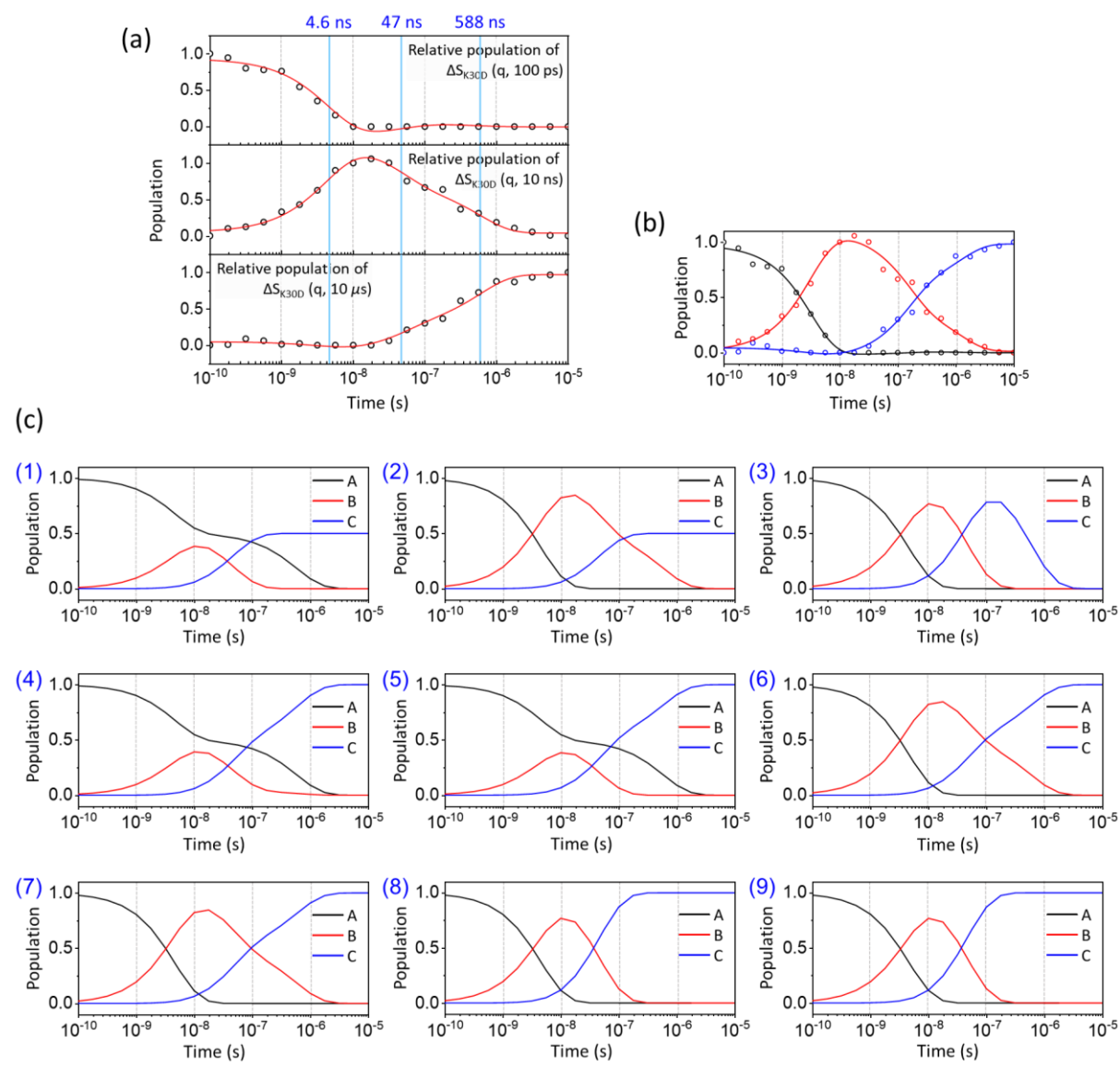


Fig. S15 (a) The SAPPA kinetic profiles obtained from SAPPA using the experimental difference curves at 100 ps , 10 ns , and $10 \mu\text{s}$ as the basis spectra to fit the relative contributions of the three basis spectra as a function of time. The relative populations indicated in empty circles are obtained from SAPPA, and the red curves are from fitting the three SAPPA kinetic profiles with the common time constants fixed at those obtained from the fit of rSVs (4.6 ns , 47 ns , 588 ns). (b) The SAPPA kinetic profiles of (a) shown in a different style to facilitate easy comparison with the kinetic profiles from candidate kinetic models of (c). The profiles of the first, second, and third basis components are shown in black, red, and blue, respectively. (c) The simulated kinetic profiles of three intermediates for the nine candidate kinetic models shown in Fig. S14. Comparison of the kinetic profiles in (c) and the SAPPA kinetic profiles in (b) show that only models (6) and (7) are compatible with the experimental data, ruling out the other models.

REFERENCES

1. K. Y. Oang, C. Yang, S. Muniyappan, J. Kim and H. Ihee, *Struct. Dyn.*, 2017, **4**, 044013.
2. W. E. Royer, Jr., R. A. Fox, F. R. Smith, D. Zhu and E. H. Braswell, *J. Biol. Chem.*, 1997, **272**, 5689-5694.
3. P. Ceci, L. Giangiacomo, A. Boffi and E. Chiancone, *J. Biol. Chem.*, 2002, **277**, 6929-6933.
4. V. Srager, T. Teng, T. Ursby, C. Pradervand, Z. Ren, S. Adachi, W. Schildkamp, D. Bourgeois, M. Wulff and K. Moffat, *Science*, 1996, **274**, 1726-1729.
5. E. Chen, M. J. Wood, A. L. Fink and D. S. Kliger, *Biochemistry*, 1998, **37**, 5589-5598.
6. V. Srager, Z. Ren, T. Y. Teng, M. Schmidt, T. Ursby, D. Bourgeois, C. Pradervand, W. Schildkamp, M. Wulff and K. Moffat, *Biochemistry*, 2001, **40**, 13802-13815.
7. F. Schotte, M. Lim, T. A. Jackson, A. V. Smirnov, J. Soman, J. S. Olson, G. N. Phillips, Jr., M. Wulff and P. A. Anfinrud, *Science*, 2003, **300**, 1944-1947.
8. M. Schmidt, K. Nienhaus, R. Pahl, A. Krasselt, S. Anderson, F. Parak, G. U. Nienhaus and V. Srager, *Proc. Natl. Acad. Sci. U. S. A.*, 2005, **102**, 11704-11709.
9. R. t. Aranda, E. J. Levin, F. Schotte, P. A. Anfinrud and G. N. Phillips, Jr., *Acta Crystallogr., Sect. D: Biol. Crystallogr.*, 2006, **62**, 776-783.
10. M. Cammarata, M. Levantino, F. Schotte, P. A. Anfinrud, F. Ewald, J. Choi, A. Cupane, M. Wulff and H. Ihee, *Nat. Methods*, 2008, **5**, 881-886.
11. S. Ahn, K. H. Kim, Y. Kim, J. Kim and H. Ihee, *J. Phys. Chem. B*, 2009, **113**, 13131-13133.
12. H. S. Cho, N. Dashdorj, F. Schotte, T. Gruber, R. Henning and P. Anfinrud, *Proc. Natl. Acad. Sci. U. S. A.*, 2010, **107**, 7281-7286.
13. S. Westenhoff, E. Nazarenko, E. Malmerberg, J. Davidsson, G. Katona and R. Neutze, *Acta Crystallogr., Sect. A: Found. Crystallogr.*, 2010, **66**, 207-219.
14. K. H. Kim, K. Y. Oang, J. Kim, J. H. Lee, Y. Kim and H. Ihee, *Chem. Commun.*, 2011, **47**, 289-291.
15. K. Y. Oang, J. G. Kim, C. Yang, T. W. Kim, Y. Kim, K. H. Kim, J. Kim and H. Ihee, *J. Phys. Chem. Lett.*, 2014, **5**, 804-808.
16. K. Y. Oang, K. H. Kim, J. Jo, Y. Kim, J. G. Kim, T. W. Kim, S. Jun, J. Kim and H. Ihee, *Chem. Phys.*, 2014, **422**, 137-142.
17. J. G. Kim, T. W. Kim, J. Kim and H. Ihee, *Acc. Chem. Res.*, 2015, **48**, 2200-2208.

18. A. Shimada, M. Kubo, S. Baba, K. Yamashita, K. Hirata, G. Ueno, T. Nomura, T. Kimura, K. Shinzawa-Itoh, J. Baba, K. Hatano, Y. Eto, A. Miyamoto, H. Murakami, T. Kumasaka, S. Owada, K. Tono, M. Yabashi, Y. Yamaguchi, S. Yanagisawa, M. Sakaguchi, T. Ogura, R. Komiya, J. Yan, E. Yamashita, M. Yamamoto, H. Ago, S. Yoshikawa and T. Tsukihara, *Sci. Adv.*, 2017, **3**, e1603042.
19. T. W. Kim, S. J. Lee, J. Jo, J. G. Kim, H. Ki, C. W. Kim, K. H. Cho, J. Choi, J. H. Lee, M. Wulff, Y. M. Rhee and H. Ihee, *Proc. Natl. Acad. Sci. U. S. A.*, 2020, **117**, 14996-15005.
20. A. Ansari, C. M. Jones, E. R. Henry, J. Hofrichter and W. A. Eaton, *Biochemistry*, 1994, **33**, 5128-5145.
21. G. Balakrishnan, M. A. Case, A. Pevsner, X. Zhao, C. Tengroth, G. L. McLendon and T. G. Spiro, *J. Mol. Biol.*, 2004, **340**, 843-856.
22. K. H. Kim, S. Muniyappan, K. Y. Oang, J. G. Kim, S. Nozawa, T. Sato, S. Y. Koshihara, R. Henning, I. Kosheleva, H. Ki, Y. Kim, T. W. Kim, J. Kim, S. Adachi and H. Ihee, *J. Am. Chem. Soc.*, 2012, **134**, 7001-7008.
23. J. G. Kim, S. Muniyappan, K. Y. Oang, T. W. Kim, C. Yang, K. H. Kim, J. Kim and H. Ihee, *Struct. Dyn.*, 2016, **3**, 023610.
24. C. Yang, M. Choi, J. Kim, H. Kim, S. Muniyappan, S. Nozawa, S.-i. Adachi, R. Henning, I. Kosheleva and H. Ihee, *Int. J. Mol. Sci.*, 2018, **19**, 3633.
25. H. Kim, J. G. Kim, S. Muniyappan, T. W. Kim, S. J. Lee and H. Ihee, *J. Phys. Chem. B*, 2020, **124**, 1550-1556.